

# We are IntechOpen, the world's leading publisher of Open Access books Built by scientists, for scientists

6,900

Open access books available

185,000

International authors and editors

200M

Downloads

Our authors are among the

154

Countries delivered to

TOP 1%

most cited scientists

12.2%

Contributors from top 500 universities



WEB OF SCIENCE™

Selection of our books indexed in the Book Citation Index  
in Web of Science™ Core Collection (BKCI)

Interested in publishing with us?  
Contact [book.department@intechopen.com](mailto:book.department@intechopen.com)

Numbers displayed above are based on latest data collected.  
For more information visit [www.intechopen.com](http://www.intechopen.com)



# Dynamic Speckle Interferometry of Thin Biological Objects: Theory, Experiments, and Practical Perspectives

Alexander P. Vladimirov and Alexey A. Bakharev

Additional information is available at the end of the chapter

<http://dx.doi.org/10.5772/66712>

## Abstract

Relation between the phase dynamics of the waves sounding thin biological object and the dynamics of the speckles in the object image plane was theoretically detected using a model dealing with interference of multiple waves with random phases. Formulas determining the dependence of time-average intensity  $\bar{I}$  and temporal autocorrelation function  $\eta = \eta(t)$  of this intensity at a point of the image plane with mean value  $\langle x \rangle$ , mean square deviation  $\sigma_u$ , and correlation time  $\tau_0$  of the difference between the optical paths  $\Delta u$  of the wave pairs in the neighborhood of a conjugate point of the object plane were obtained. A relation between a normalized temporal spectral function of stationary process  $\Delta u(t)$  and a temporal spectral radiation intensity fluctuation function was substantiated. An optical device relevant to the model used in the theory was developed. Good quantitative coincidence between the theory and the experiment was shown by means of dosed random variation of path difference  $\Delta u$ . The calibration procedure for the device determining  $\sigma_u$  was developed; errors and the sensitivity limit of the technique were assessed. Application of value  $\sigma_u$  as a cell activity parameter on biological objects, namely, a monolayer of live cells on a transparent substrate in a thin cuvette with the nutrient solution was substantiated. It was demonstrated that the technique allows determination of herpes virus in the cells as early as 10 min from the experiment start. A necessity to continue upgrading of the technique was pointed out as well as its prospects for studying the cell reaction to toxic substances, bacteria, and viruses considered.

**Keywords:** interference, speckle, speckle dynamics, phase object, live cells, cell activity, viruses

## 1. Introduction

If a rough object is illuminated at some angle or a transparent object is illuminated by coherent radiation via matte glass, an inhomogeneous or a speckle is generated in the image plane. Speckles of random brightness and size are generated as a result of mutual interference of multiple waves with random amplitudes and phases. A random radiation intensity value at any point of the image plane can be regarded as resulting from superposition of multiple waves arriving from the area in the neighborhood of the conjugate point in the object plane. Minimum transverse speckle size  $2b_s$  is related to the linear resolution of the lens  $2a_s$ , with formula  $a_s = b_s/m$ , where  $m$  is magnification generated by the lens.

At present, the statistic properties of stationary speckles have been well studied, and they can be checked for in various publications [1–4].

If the phases of sounding waves vary due to the processes occurring on the surface of the reflecting object or inside a transparent body, the speckle pattern will vary. Speckle dynamics manifests itself as a speckle shift and (or) a change of their structure. At present, there are numerous papers on application of this phenomenon and interference of speckle fields during studies of solid, liquid, or gaseous mediums [5–10].

The speckles generated by biological objects have been called biospeckles in the literature. Some researchers mean that biospeckles are speckle dynamics due to the processes occurring in biological objects. Below, we are going to regard biospeckles as speckles generated by biological objects.

There is vast literature on the properties of biospeckles generated by various objects: seeds, fruit, vegetables, plant leaves, bacteria, skin, patients' extremities, etc. Numerous examples of such studies can, for example, be found in a monograph [11]. Despite a large number of publications on biospeckles, there is just one technique implemented in clinical practice. This technique was originally proposed in Ref. [12], and it permits determination of the blood flow velocity in the blood vessels of the patients' retinas or extremities. The latest publications aiming at upgrading of the technique can be checked for in Ref. [13]. Successful application of this technique might be related to the fact that authors developed its theory at a certain stage of the research [14].

When live cells are sounded by coherent waves, the intracellular processes can alter the amplitudes and phases of the waves, thus changing the speckle image of an object. This provides an opportunity to study intracellular processes by the features of biospeckle dynamics in principle so that, for example, the problem of therapeutic drug management could be solved. That is why establishing of the relation between the physical-chemical intracellular processes and the biospeckle dynamics is a task vital both from the scientific and practical point of view. The authors explain absence of notable progress in solution of this problem by absence of a theory establishing a relation between the parameters that characterize the physical-chemical processes influencing the variation of the cell-sounding wave phases and the parameters characterizing speckle dynamics. Recently, one of the authors of this paper developed a similar theory for thin biological object so that this paper aims at familiarizing the

readers with the adopted model, the results of the theory test on the model objects, and with some perspectives of its application.

## 2. Interference of two and multiple waves

### 2.1. Complex amplitude of light wave and radiation intensity

The electromagnetic nature of the light waves was theoretically substantiated by British physicist Maxwell in his paper [15]. Ruling out the currents from his equation system, he obtained an equation that describes the propagation of electromagnetic disturbances:

$$\Delta \vec{f} - \frac{1}{c^2} \frac{d^2 \vec{f}}{dt^2} = 0, \quad (1)$$

where  $\vec{f}$  is the electric  $\vec{E}$  or magnetic  $\vec{H}$  field vector tension, and  $c$  is light velocity.

Note that this equation exactly coincides with the equation of disturbance motion in elastic no compressive medium.

Further, let us target on plane monochrome waves that are a special case of a solution to Eq. (1). These are the waves wherein the electric and magnetic field vary according to the cosine law and vector  $\vec{f}$  is a function of a single coordinate and time. Let us restrict ourselves to discussing the tension of the electric-field vector. In a form independent from the origin selection for a plane monochrome wave, we have [16]:

$$\vec{E} = \text{Re} \left\{ \vec{E}_0 e^{i(\vec{k} \cdot \vec{r} - \omega t)} \right\}, \quad (2)$$

where  $\vec{E}_0$  is some constant complex vector,  $\vec{k}$  is a wave vector equaling  $(\omega/c) \vec{n} = (2\pi/\lambda) \vec{n}$ ,  $\vec{r}$  is a radius vector of a point of space,  $\omega$  is the wave frequency,  $\lambda$  is the wavelength, and  $\vec{n}$  is a single vector coinciding with the direction of the light wave propagation.

Let us further accept that all the waves have the same direction of the electric field vectors, then, when the waves impose their amplitudes, they can be added as scalar values. Besides, further in Eq. (2), we shall omit symbol  $\text{Re}$  and operate exponents instead of cosines. It is possible because in the problems that we are discussing below the final result will differ by an insufficient factor. Instead of Eq. (2), we have:

$$E(x, y, z, t) = A(x, y, z) \exp(-i\omega t), \quad (3)$$

where expression  $A(x, y, z) = |A(x, y, z)| \exp[i\theta(x, y, z)]$  was named complex amplitude in optics,  $|A(x, y, z)|$  is the module of the complex amplitude, and  $\theta(x, y, z)$  is the wave phase at the observation point.

Now let us introduce the notion of light intensity as a value proportionate to volumetric density of radiation energy averaged by the time interval substantially exceeding the wave oscillation period:

$$I(x, y, z) = \lim_{T \rightarrow \infty} \frac{1}{T} \int_{-T/2}^{T/2} |E(x, y, z, t)|^2 dt = |A(x, y, z)|^2. \quad (4)$$

Thus, the radiation intensity at a point of space equals the squared complex amplitude module.

## 2.2. Interference of two waves

Let us discuss the light intensity distribution in superposition of two monochrome waves. Suppose that two waves of the same length  $\lambda$  were emitted by one point source in various directions, then two plane waves 1 and 2 crossing at angle  $\theta$  were shaped by the optical systems. Let us take some point in the area of beam superposition. For certainty, let the wave amplitudes be the same equaling  $A_0$ , but their initial phases  $\varphi$  differ. In compliance with Eq. (4), we have:

$$\begin{aligned} I = A \times A^* &= \left[ A_0 e^{i(\vec{k}_1 \vec{r} + \varphi_1)} + A_0 e^{i(\vec{k}_2 \vec{r} + \varphi_2)} \right] \times \left[ A_0 e^{-i(\vec{k}_1 \vec{r} + \varphi_1)} + A_0 e^{-i(\vec{k}_2 \vec{r} + \varphi_2)} \right] \\ &= 2I_0 + 2I_0 \cos \left[ (\vec{k}_1 - \vec{k}_2) \vec{r} + \varphi_1 + \varphi_2 \right], \end{aligned} \quad (5)$$

where  $I_0 = A_0^2$ . Eq. (5) describes periodic light intensity distribution in the neighborhood of point  $\vec{r}$ , which was called light interference by T. Jung. Elementary calculations can demonstrate [17, 18] that minimum distance  $\Delta$  between neighboring intensity maximums or minimums called bandwidth or period of the interference fringes is determined by formula (Eq. (6)):

$$\Delta = \frac{\lambda}{2 \sin \frac{\theta}{2}}. \quad (6)$$

It follows from Eq. (6) that if  $\theta$  tends to zero,  $\Delta$  tends to infinity, which corresponds to tuning of the interferometer to “endless” band. If angle  $\theta$  between vectors  $\vec{k}_1$  and  $\vec{k}_2$  equals  $180^\circ$ , then  $\Delta = \lambda/2$ , which corresponds to the wave interference in colliding beams. For  $\theta = 60^\circ$  value,  $\Delta = \lambda$ .

Now let us discuss the contrast of the interference fringes  $\gamma$  introduced by Michelson and determined by formula  $\gamma = (I_{\max} - I_{\min}) / (I_{\max} + I_{\min})$ , where  $I_{\min}$  and  $I_{\max}$  are the minimum and the maximum intensity values, respectively. From Eq. (5), it follows that in the case of a point light source discussed here and constant wavelength  $\lambda$ , contrast  $\gamma = 1$ . Experience shows that if the light source is not point and (or) it emits light in some wavelength interval, the fringes contrast is less than 1.

It is commonly believed that case  $\gamma = 0$  corresponds to completely incoherent light; if  $0 < \gamma < 1$ , the light is partially coherent, and coherence is the ability of waves to interfere. Interference of partially coherent light can be studied in Ref. [19]. In the text below, we will suppose that the light waves discussed here are completely coherent, i.e., two waves of the

same amplitude generate an interference pattern with the contrast equal to 1. We can suppose with practical precision that similar waves are generated by laser light sources.

### 2.3. Interference of multiple waves with random amplitudes and phases

The creation of laser and discovery of the speckle structure of scattered radiation were immediately followed by a number of theoretical papers on statistical properties of speckles in free space [1] and in the image area of scattering surface [2]. **Figure 1** presents a typical speckle pattern observed in the image plane of a rough surface. The picture was obtained by the authors of this manuscript during its preparation. In this section, we discuss some main features of speckle fields obtained by Goodman [3, 4] on a simple model describing interference of multiple waves.

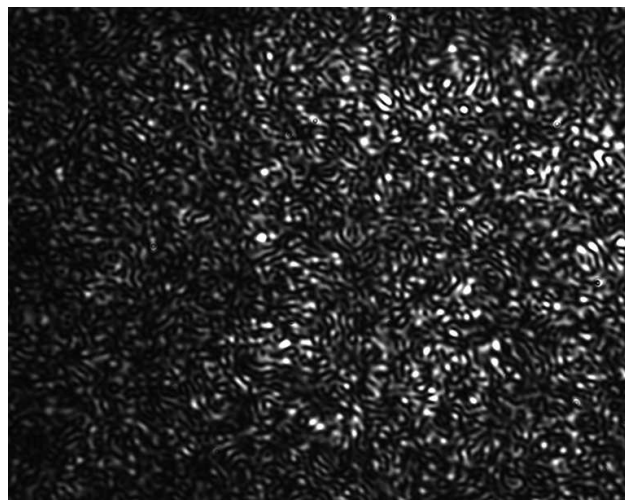


**Figure 1.** Speckles in the image plane of a rough surface.

According to Goodman's model, the waves that arrived at an arbitrary point of the free space from elementary areas of surface can be regarded as plane monochrome waves with random amplitudes  $a_j/\sqrt{N}$  and phases  $\varphi_j$ , where  $j$  is the wave number,  $j = 1, 2, \dots, N$ . It was supposed that the amplitude and phase of the same wave and the amplitudes and phases of different waves are independent, and the values of  $a_j^2$  averaged by the object ensemble are nonzero. It was considered that phases  $\varphi_j$  were homogeneously distributed in the area from  $-\pi$  to  $+\pi$ . The presence of the object ensemble means the presence of numerous macroscopically identical scattering objects, each object generating  $N$  plane and monochrome waves with random amplitudes and phases. Any value averaged by the object ensemble is found by means of fixation for every object of the ensemble with subsequent calculation of its mean value. In the text below, we will denote the ensemble-average with angular parenthesis. Note that mathematically, object ensemble-averaged value of some function  $f$  of random arguments  $x_1, x_2, \dots, x_m$ , is determined in the following way:



$$\langle f(x_1, x_2, \dots, x_m) \rangle = \int_{-\infty}^{+\infty} \dots \int_{-\infty}^{+\infty} f(x_1, x_2, \dots, x_m) \rho(x_1, x_2, \dots, x_m) dx_1 dx_2 \dots dx_m, \quad (7)$$

where  $\rho(x_1, x_2, \dots, x_m)$  is joint probability density of random values  $x_1, x_2, \dots, x_m$ . If these values are independent,  $\rho(x_1, x_2, \dots, x_m) = \rho(x_1)\rho(x_2)\dots\rho(x_m)$ , and the calculation of integral (Eq. (7)) may simplify substantially.

If all the waves are linearly polarized in the same mode, then, according to J. Goodman, the following ratio holds for total complex amplitude  $A$  at some point  $\vec{q}$  of the free space:

$$A = ae^{-i\theta} = A^r + iA^i = \frac{1}{\sqrt{N}} \sum_{j=1}^N a_j e^{i\varphi_j}, \quad (8)$$

where  $A^r$  and  $A^i$  are real and imaginary parts of the total complex amplitude, respectively. Eqs. (9)–(11) obtained by Goodman on the basis of the discussed model that characterize the statistical properties of speckles are cited as follows:

$$\langle A^r \rangle = \langle A^i \rangle = \langle A^r A^i \rangle = 0, \quad (9)$$

$$\langle A^r A^r \rangle = \langle A^i A^i \rangle = \frac{1}{2N} \sum_{j=1}^N \langle a_j^2 \rangle, \quad (10)$$

$$\rho(A^r A^i) = \frac{1}{2\pi\sigma^2} e^{-\frac{(A^r)^2 + (A^i)^2}{2\sigma^2}}, \quad (11)$$

$$\rho(I, \theta) = \rho(I) \times \rho(\theta) = \frac{1}{\langle I \rangle} e^{-\frac{I}{\langle I \rangle}} \times \frac{1}{2\pi}, \quad I \geq 0, \quad -\pi \leq \theta \leq \pi, \quad 2\sigma^2 = \langle I \rangle, \quad (12)$$

$$\langle I^n \rangle = n! \langle I \rangle^n. \quad (13)$$

From Eqs. (9)–(13), it follows that at an arbitrary point of a free field, the real and imaginary parts of total complex amplitudes are independent, uncorrelated, and distributed according to the Gauss' law. Radiation intensity  $I$  and resulting phase  $\theta$  are independent, value  $\theta$  is homogeneously distributed in the range from  $-\pi$  to  $+\pi$ . From Eq. (12), it follows that probability  $P_I$  exceeding some threshold equal to  $I$  by the light intensity that is given by Eq. (14):

$$P_I = e^{-\frac{I}{\langle I \rangle}} \quad (14)$$

Thus, in a speckle field, the most probable intensity value is value  $I$  equal to zero. With increasing intensity, the probability of its detection decreases exponentially. From Eq. (13), it also follows that speckle contrast  $C$  equal to the ratio of mean square deviation intensity to the mean intensity equals 1.

Experience shows that experimental dependence  $P_I(I)$  agrees well with theoretical dependence Eq. (14) for scattering surfaces that lack the mirror constituent of scattered radiation, and whose height of heterogeneity of the surface relief is comparable with wavelength  $\lambda$ . The

statistical properties of the speckles corresponding to other models of rough surface can be studied, for example, in Refs. [20, 21].

The model proposed by Goodman was further developed in Ref. [22] to obtain the formula allowing determination of three-dimensional speckle sizes. It was supposed that point scattering centers were located in some three-dimensional area transparent for radiation. A formula was obtained that allowed determination of three-dimensional speckle sizes for an area of an arbitrary shape with random location of the radiation source, the object, and the observation site by the width of a spatial autocorrelation function of intensity of scattered radiation. The formulas determining the transverse and longitudinal speckle sizes for two objects of a simple shape are given below. Let us examine a transparent area shaped like a right-angle parallelepiped of size  $2X$  and  $2Y$  on  $ox$  and  $oy$  axes, respectively, and of size  $2Z$  on  $oz$  axis. Point scatterers are located within the area. Let the coordinate origin be located in the center of the area. Then, if the direction of illumination is arbitrary at distance  $\rho_q$  on  $oz$  axis, speckles with minimum sizes  $\Delta\tilde{q}_x$ ,  $\Delta\tilde{q}_y$ ,  $\Delta\tilde{q}_z$  are generated as  $xd$ ,  $yd$ , and  $zd$ , respectively:

$$\Delta\tilde{q}_x = \frac{\lambda\rho_q}{2X}, \Delta\tilde{q}_y = \frac{\lambda\rho_q}{2Y}, \Delta\tilde{q}_z = \frac{5\lambda\rho_q^2}{\pi(X^4 + Y^4)^{1/2}}. \quad (15)$$

If the object is cylindrical, axis  $oz$  coincides with the axis of the cylinder, and the coordinate origin is located in the center of the object, then in similar observation and illuminating conditions

$$\Delta\tilde{r} = 1.22 \frac{\lambda\rho_q}{D}, \Delta\tilde{q}_z = 2 \frac{\lambda\rho_q^2}{R^2}, \Delta r = (\Delta q_x^2 + \Delta q_y^2)^{1/2}, \quad (16)$$

where  $R$  is the radius of the cylinder,  $D = 2R$ . In the literature [5, 23], it was shown that the mean  $xd$ ,  $yd$ , and  $zd$  speckle sizes are threefold compared with the minimum.

In the preceding text above, we confined ourselves to the main features of speckle fields in a free field. The speckles generated in the scattering image plane have very similar properties. For the speckles in the area of the object images in Eqs. (15) and (16), values  $2X$ ,  $2Y$ , and  $R$  equal the size of a diaphragm of the relevant shape located near the lens.

### 3. Theory of dynamic speckle interferometry of thin phase objects

To study various properties of transparent objects, a variety of interference, shadow and speckle techniques are conventionally used [24–26]. As a rule, these techniques are oriented toward the analysis of macroscopic processes. With that, the logic of advancement in speckle optics and the practical needs pose the problem of studying microscopic processes occurring at the structure level. In particular, in biology, the problem of therapeutic drug management poses the problem of studying the processes in cells and their membranes. As at the structure level, the properties of biological media are random, when waves pass through various parts of the cell, their phase randomly varies in time. Therefore, a variation of the radiation intensity



at the observation point is also a random process. The complexity of theoretical analysis of similar phenomena is that in the general case, there is necessity for dispersive ratios characterizing the wave phase variation in space and time.

In practice, there is an option when random values of the wave phases varying in space and time are independent. In particular, this option may be generated if the area of spatial correlation of a physical value causing the wave phase variations is less than the wavelength of light  $\lambda$ . In this case, the solution to the problem of establishing a relation between the wave phase dynamics in a thin transparent (phase) object and the dynamics of the light intensity in its image plane simplifies considerably. The solutions to this problem attempted for studying the properties of particular objects are found in the literature [27, 28]. In the para below, we are giving the general solution to the problem obtained by the authors of this paper.

### 3.1. Model of the object

At the first stage, the aim of the theoretical analysis is to obtain the expression for radiation intensity  $I(\vec{q})$  at some point  $\vec{q}$  of the observation plane, and then for temporal autocorrelation function of a random process  $I = I(t)$ . We will obtain the expression for value  $I(\vec{q})$  using the model of a three-dimensional diffuser published in the abovementioned paper [22]. Let a point source of coherent radiation with wavelength  $\lambda$  located at point 1 illuminate point scattering centers randomly located in thin diffuser 2 near  $(xoy)$  plane as is shown in **Figure 2**. Let the position of the point source be given by radius vector  $\vec{s}$ . To simplify the transformations, let us admit that the refraction indexes of the medium inside and outside the diffuser are the same and equal 1. At distance  $L_0$  from  $(xoy)$  plane, in plane  $(\beta_x 0 \beta_y)$  there is a thin lens with focal distance  $f$  and diaphragm diameter  $D$ . Planes  $(xoy)$  and  $(q_x 0 q_y)$  are conjugate. We consider all the waves discussed linearly polarized in the same direction. Let us admit that phase  $\varphi_j$  of the wave scattered by the  $j$ th center is random, and the waves from all the scattering centers arrive at an arbitrary point of  $(\beta_x 0 \beta_y)$  plane.

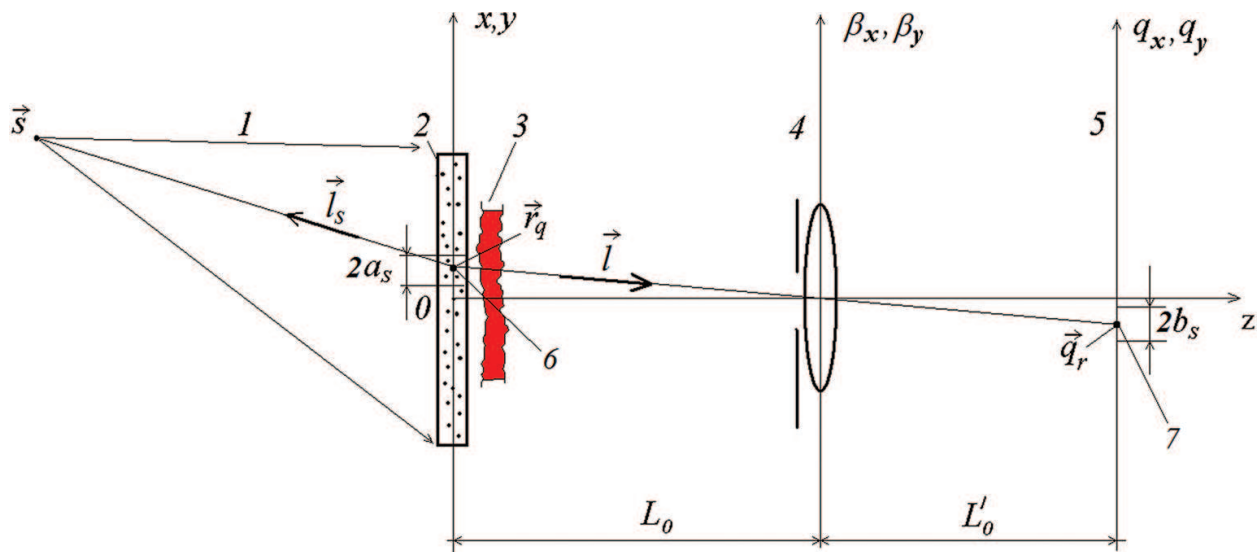


**Figure 2.** Optical system taken in the theory: (1) light source, (2) diffuser, (3) thin transparent object, (4) the lens with diaphragm, (5) the image plane, (6,7) conjugate points.

Let thin phase object 3 whose refraction index varies in time (**Figure 2**) be located near the diffuser to its right. Let us admit that the longitudinal resolution of the lens exceeds the sum of the diffuser thickness, the object thickness, and the distance from the object to the diffuser. We also suggest that the point scattering centers are fairly rare, so the random phases of the waves that have passed through the object are independent.

### 3.2. Radiation intensity

First, let us obtain the expression for radiation intensity  $I(\vec{q})$  at some point  $\vec{q}$  of plane  $(q_x 0 q_y)$  in the absence of the phase object. We suppose that the optical system does not permit separate scattering centers, and that the number of the scattering centers is fairly large in the area of the transverse lens resolution. For total complex amplitude  $A(\vec{\beta})$  at arbitrary point  $\vec{\beta}$  of plane  $(\beta_x 0 \beta_y)$  we have:

$$A(\vec{\beta}) = \sum_{j=1}^M a_j(\vec{\beta}), \quad (17)$$

where  $M$  is the count of scattering centers,  $a_j(\vec{\beta})$  is the complex amplitude of the  $j$ th wave at point  $\vec{\beta}$ . We will obtain the complex amplitude of light  $A(\vec{q})$  at point  $\vec{q}$  adding the amplitudes of waves that arrived from the points of plane  $(\beta_x 0 \beta_y)$  to point  $\vec{q}$ , taking amplitude  $P(\vec{\beta})$  and phase  $\exp ik|\vec{\beta}|/2f$  lens transmission into consideration [7]:

$$A(\vec{q}) = \int_{-\infty}^{+\infty} \int P(\vec{\beta}) e^{\frac{ik|\vec{\beta}|}{2f}} e^{ik|\vec{L}_q(\vec{\beta})|} \sum_{j=1}^M a_j(\vec{\beta}) d\beta_x d\beta_y, \quad (18)$$

where  $i$  is an imaginary unit,  $k = 2\pi/\lambda$  is the wave number, and  $\vec{L}_q(\vec{\beta})$  is the vector connecting points  $\vec{\beta}$  and  $\vec{q}$ . Henceforward, the inferior index of the vector denotes the position of the vector head.

Let us take the relation between the complex amplitude of light in proximity to point  $\vec{r}_j$  and at point  $\vec{\beta}$  in the same form as in Ref. [7]:

$$a_j(\vec{\beta}) = \sqrt{I_0(\vec{r}_j)} \xi(\vec{r}_j) e^{i\{k[|\vec{L}_s(\vec{r}_j)| + |\vec{L}_\beta(\vec{r}_j)|] + \varphi_j\}}, \quad (19)$$

where  $I_0 = I_0(\vec{r})$  is a distribution of the illuminating radiation intensity,  $\xi = \xi(\vec{r})$  in the general case is a complex coefficient accounting the share of the radiation going from point  $\vec{r}$  to point  $\vec{\beta}$ ,  $\vec{L}_s(\vec{r})$  is the vector connecting points  $\vec{r}$  and  $\vec{s}$ , and  $\vec{L}_\beta(\vec{r})$  is the vector connecting points  $\vec{r}$  and  $\vec{\beta}$ .

Let us take arbitrary point 6 in plane  $(xoy)$  and its conjugate point 7 in plane  $(q_x 0 q_y)$  that are given by radius vectors  $\vec{r}_q$  and  $\vec{q}_r$ , respectively (**figure 2**). It is known that the wave going from point 6

generates an Airy pattern with the center in point 7 as the result of light diffraction on the diaphragm of diameter  $D$ . The radius of the central spot  $b_s$  of the pattern equals  $1.22\lambda L'_0/D$ , where  $L'_0$  is the distance from the lens to plane  $(q_x 0 q_y)$ . The areas of radius  $b_s$  in plane  $(xoy)$  correspond to the area of radius  $a_s = b_s/m$ , where  $m$  is the magnification generated by the lens. It is known that 85% of the energy of the wave that passed through the lens falls on the central speckle of the Airy pattern. We are going to neglect the energy of the waves beyond the area of radius  $b_s$ . This in turn means that we suppose that the waves only from the scattering centers in the area of radius  $a_s$  with the center at point 6 arrive at point 7. Let  $N$  be the number of these centers.

Then, supposing that the area of radius  $a_s$ , the thickness of the diffuser and value  $D$  are small compared to the distances from the object to the radiation source and to the lens, and also from the lens to the image plane, we can obtain the expression for complex amplitude  $A(\vec{q})$ :

$$A(\vec{q}) = \sqrt{I_0} e^{i\psi} \sum_{j=1}^N e^{i\theta_j}, \quad (20)$$

where  $I_0, \psi$  are constants,  $\theta_j = k\vec{r}_j(\vec{l}_s + \vec{l}) + \varphi_j$ ,  $\vec{l}_s = \vec{l}_s(l_{sx}, l_{sy}, l_{sz})$  and  $\vec{l} = \vec{l}(l_x, l_y, l_z)$  are single vectors directed from point  $\vec{r}_q$  toward the radiation center and to the observer, respectively, complex amplitude  $\sqrt{I_0} e^{i\psi}$  determines the complex expression preceding the summation sign. A detailed output of Eq. (20) can be found in Ref. [29].

Let us insert a thin phase object between the diffuser and the lens, as shown in **Figure 2**. Let us suppose that the object will alter only the phase of the  $j$ th wave, and there is no light refraction. In this case value,  $\theta_j$  will change by value  $\zeta_j$ , where

$$\zeta_j = \frac{2\pi}{\lambda} \left\{ \int_{l_j} [n_j(l) - n_0] dl \right\} = \frac{2\pi}{\lambda} u_j, \quad (21)$$

$n_j(l)$  is a distribution of the refraction index in the phase object along the path of the  $j$ th wave,  $l_j$  is the path length of the  $j$ th wave in the object; integrals are found along the wave path,  $u_j$  is the optical difference of the  $j$ th wave travel path in the phase object.

So instead of Eq. (20), we have:

$$A(\vec{q}) = \sqrt{I_0} e^{i\psi} \sum_{j=1}^N e^{i(\zeta_j + \theta_j)} \quad (22)$$

For radiation intensity at point  $\vec{q}$  we have the following:

$$I(\vec{q}) = A(\vec{q})A^*(\vec{q}) = I_0 \sum_{j=1}^N \sum_{m=1}^N e^{i[k(u_j - u_m) + \theta_j - \theta_m]} = I_0 N + 2I_0 \sum_{\kappa=1}^K \cos[k\Delta u_\kappa + \Delta\theta_\kappa], \quad (23)$$

where  $\Delta u_\kappa$  is the relative optical difference of the travel path of the  $\kappa$ th pair of scattering centers,  $\Delta\theta_\kappa = \theta_j - \theta_m$ ,  $j \neq m$ ,  $\kappa = 1, 2, \dots, K$ ,  $K = N(N-1)/2$ .

### 3.3. Temporal autocorrelation function

First, let us obtain the expression for temporal autocorrelation function of the radiation intensity at point  $\vec{q}$ , i. e., Eq. (24):

$$R_{1,2}(t_1, t_2) = \langle [I_1 - \langle I_1 \rangle] \times [I_2 - \langle I_2 \rangle] \rangle = \langle I_1 I_2 \rangle - \langle I_1 \rangle \langle I_2 \rangle, \quad (24)$$

where inferior indexes 1 and 2 denote time points  $t_1$  and  $t_2$ , angle parentheses denote averaging by the object (model) ensemble. Let us suggest that at different  $\kappa$  random values  $\Delta u_\kappa$  are independent, and at the same  $\kappa$ , their time correlation occurs. Suppose also that joint probability density  $\rho(\Delta u_{\kappa 1}, \Delta u_{\kappa 2})$  is a two-dimensional Gaussian function that is the same for different  $\kappa$ . So further we are going to omit inferior index  $\kappa$  in expressions  $\Delta u_\kappa$ . Using the suggestions made in Ref. [29], we obtained the expression for  $R_{1,2}(t_1, t_2)$ :

$$R_{1,2}(t_1, t_2) = I_0^2 N(N-1) \cos[(\langle x_2 \rangle - \langle x_1 \rangle)] \times e^{-\frac{1}{2}k_{11} - \frac{1}{2}k_{22} + k_{12}}, \quad (25)$$

where  $\langle x_1 \rangle$  and  $\langle x_2 \rangle$  are the object ensemble-averaged values  $x = k\Delta u$  at time points  $t_1$  and  $t_2$ , respectively,  $k_{11}$  and  $k_{22}$  are dispersions of value  $x$  at time moments  $t_1$  and  $t_2$ , respectively,  $k_{12} = \langle (x_1 - \langle x_1 \rangle)(x_2 - \langle x_2 \rangle) \rangle$ . For the normalized autocorrelation function  $\eta_{12} = R_{12}(t_1, t_2)/R_{12}(t_1, t_1)$  we have the following:

$$\eta_{12} = \cos[(\langle x_2 \rangle - \langle x_1 \rangle)] \times e^{-\frac{1}{2}k_{11} - \frac{1}{2}k_{22} + k_{12}}. \quad (26)$$

Let process  $x = x(t)$  be stationary. Then  $\langle x_1 \rangle = \langle x_2 \rangle$ ,  $k_{11} = k_{22}$  and, therefore,

$$\eta(\tau) = e^{-k_{11} + k_{11}\rho_{12}(\tau)}, \quad (27)$$

where  $\tau = t_2 - t_1$ ,  $\rho_{12}(\tau)$  is a normalized temporal correlation function of random value  $k\Delta u$ . Let  $\rho_{12}(\tau) \rightarrow 0$ ,  $\tau \rightarrow \infty$ . For example, this is a feature of normalized Lorentzian and Gaussian correlation functions. Then function  $\eta(\tau)$  levels off to  $\eta^*$  equal to  $\exp(-k_{11})$ . So by value  $\eta$  leveling off with time, we can determine dispersion  $k_{11}$  of phase differences varying in time and variation  $\sigma_u = \frac{\lambda}{2\pi} \sqrt{k_{11}}$  of value  $\Delta u$ . We used this fact in experiments studying the processes occurring in live cells. These experiments will be discussed in Sections 5 and 6.

### 3.4. Temporal spectral function

Subtracting constant component  $\eta^*$  from Eq. (27) and renormalizing it, we obtain a new temporal autocorrelation function of radiation intensity fluctuation  $\eta'(\tau)$ :

$$\eta'(\tau) = \frac{\eta(\tau) - \eta^*}{1 - \eta^*}. \quad (28)$$

Let  $\Delta u \ll \lambda$ . Then it easy to demonstrate that  $\eta'(\tau) \approx \rho_{12}(\tau)$ . Therefore, the temporal autocorrelation function of intensity fluctuations corresponds to the temporal autocorrelation function of the wave pair optical path differences. Let us further suppose that random process

$\Delta u = \Delta u(t)$  is not only stationary but also ergodic. As the normalized temporal energetic spectrum for these processes is Fourier's transformation from the normal autocorrelation function, the corresponding normalized temporal spectral functions of intensity fluctuations  $g_{\Delta I}(\omega)$  and optical path differences  $g_{\Delta u}(\omega)$  are equal.

It was also demonstrated in Ref. [29] that if  $\Delta u \geq \lambda$  and  $\rho_{12}(\tau)$  is a Gaussian function, functions  $g_{\Delta u}(\omega)$  and  $g_{\Delta I}(\omega)$  are also Gaussian functions, but spectrum width  $g_{\Delta I}(\omega)$  is  $k_{11}$ -fold spectrum width  $g_{\Delta u}(\omega)$ . So at  $k_{11}$  increasing spectrum  $g_{\Delta I}(\omega)$  widens, and at  $\Delta u \geq \lambda$  it widens  $k_{11}$ -fold.

### 3.5. Time averaging technique

A disadvantage of the theory presented in the Section 3.4 is the difficulty of application in the case when the wave phase variations in time happen due to existence of various processes occurring simultaneously at different scale levels. For example, when the target of research is a cell, sounding wave phase variation can occur due to passage of ions via the membrane, to capture large molecules by endocytosis (local variation of the cell shape), due to chemical processes during protein synthesis in the cytoplasm and nucleus of the cell, so in Ref. [30] the technique was upgraded to overcome this disadvantage. The idea was in the application of time-averaging procedure for speckle dynamics. If characteristic time  $\tau_0$  of wave phase variation corresponding to the most rapid process is known, averaging time  $T$  of the recorded optical signals can be taken as a value exceeding  $\tau_0$ . In this case, the speckle dynamics will result from slower processes, and interpretation of the experimental data can get simplified. In the para below the results obtained in Ref. [30] are presented in brief.

Using the model discussed in Section 3.1, we obtained expressions for time-average intensity  $\tilde{I}(\vec{q})$  at point  $\vec{q}_r$  (**Figure 2**). Having substantiated the possibility of discussing continuous function  $\tilde{I} = \tilde{I}(t)$  at point  $(\vec{q})$ , we obtained the expression for temporal autocorrelation function  $R_{1,2}(t_1, t_2)$  of time-average intensity:

$$\tilde{I}(\vec{q}) = I_1 + I_2 e^{-k^2 \sigma^2 / 2} \cos(k\mu + \alpha), \quad (29)$$

$$R_{1,2}(t_1, t_2) = I^2 N(N-1) C_0^2 \cos[\langle x_2 \rangle - \langle x_1 \rangle] \times e^{-\frac{1}{2}k_{11} - \frac{1}{2}k_{22} + k_{12}}. \quad (30)$$

In Eq. (29)  $I_1$ ,  $I_2$ ,  $\alpha$  are constants,  $\mu$  and  $\sigma^2$  are mean value and dispersion of variable  $\Delta u$  obtained by time-averaging and averaging by a region of radius  $a_s$  (see **Figure 2**). Eq. (30) coincides with Eq. (25) to a precision of insufficient coefficients  $I^2$  and  $C_0^2$ . But now  $x = k\mu$ , so the arguments of the cosine and the exponent contain mean values, dispersions, and the correlation moment of a new value  $x = k\mu$ .

The peculiarity of Eq. (30) is that if averaging time  $T$  of the radiation intensity exceeds the correlation time of value  $\mu$ , normalized function, Eq. (30) takes on the following appearance:



$$\eta(\vec{q}, t_1, t_2) = \frac{R_{1,2}(\vec{q}, t_1, t_2)}{R_{1,2}(\vec{q}, t_1, t_2)} = \cos[\langle x_2 \rangle - \langle x_1 \rangle] e^{-k_{22}/2 + k_{11}/2}. \quad (31)$$

Supposing in Eq. (31) that values  $k_{11}$ ,  $k_{22}$ , and  $k\mu$  are small compared with 1, let us decompose Eq. (31) into Taylor's series in the neighborhood of points  $k_{22}$  and  $k\mu$  equal to zero, having retained the first-order derivatives. We obtain

$$\eta(t) = 1 - \frac{(k_{22}(t) - k_{11})}{2}, \quad (32)$$

where  $t = t_2 - t_1$ . It is seen from the formula that if averaging time  $T$  exceeds the correlation time of random value  $k\mu$ , the relation between  $\eta$  and  $k_{22}$  is linear.

Now among  $N$  waves let us have two wave groups with random optical wave path variations  $u_n = u_n(t)$  occurring homogeneously in the statistical sense. Let count  $n$  of such waves in groups 1 and 2, respectively, equal  $N_1$  and  $N_2$ . In practice, groups 1 and 2, for example, lie inside and outside a live cell. At large magnifications, such groups can lie within the cell nucleus and in its cytoplasm. In Ref. [30], it was shown that in this case time-average radiation intensity at conjugate point  $\vec{q}_r$  is determined by Eq. (33):

$$\tilde{I}(\vec{q}) = \tilde{I}_1 + \tilde{I}_2 + 2\tilde{I}_{12}\cos[k\Delta\mu + \theta], \quad (33)$$

where  $\tilde{I}_1$  and  $\tilde{I}_2$  are time-average intensities generated by groups 1 and 2 individually,  $\tilde{I}_{12} = I_3 e^{-\sigma_1^2/2 - \sigma_2^2/2}$  and  $I_3$ ,  $\theta$  are constants,  $\Delta\mu$  is the difference of time-average values  $u_n$  in groups 1 and 2,  $\sigma_1^2$  and  $\sigma_2^2$  are dispersions of values  $u_n$  in groups 1 and 2, respectively.

### 3.6. Relation between the object features and the parameters of speckle dynamics

We used the results of the theory presented in Section 3 to conduct experiments with live cells cultured or precipitated on a transparent substrate. To determine the value  $\eta$ , we took segments of diameter  $2a_s$  in the object plane. We regarded a region containing a large number of such segments as an object ensemble. The corresponding segments of the speckle image in the conjugate region were recorded at time points  $t_1$  and  $t_2$ , and then they were used to determine correlation coefficient  $\eta$  of digital speckle images.

Analysis of the formulas obtained demonstrates that experimentally obtained dependences  $\eta(t)$  and (or)  $\tilde{I}(t)$  can in principle be used to determine the mean value, variation, and correlation time of the medium refraction index in small regions of the transparent object. In turn, the refraction index is related to medium density  $\rho$  and its specific refractivity  $\hat{r}$  via Lorentz-Lorenz formula for liquids. For multicomponent media, the latter is equal to the sum of the products  $\hat{r}$  of single molecules on their relative concentration.



It is known that the density of liquids depends on their temperature. Therefore, if the time range where the composition of the medium can be considered constant is selected, under certain conditions the spectrum of intensity fluctuations can be regarded as the energetic spectrum of chemical reactions occurring in the cell areas under study. Similarly, if a time range or the object segments with the temperature (density) that can be considered invariable is selected, the processes of mass transfer in live cells can be studied by variation of correlation coefficient  $\eta$  or average intensity  $\tilde{I}(t)$ .

## 4. Cultured cells as research target

### 4.1. Features and advantages of cultured cells

Cell cultures have been playing a more important and notable role in toxicological, pharmacological, and other investigations. That said, the sphere of their application has been widening, and the technique of *in vitro* culture has been getting upgraded and automated. Cell cultures are single cell groups grown in invariable conditions. Moreover, the researcher is allowed to vary these conditions within certain limits enabling themselves to assess the effect of various factors such as pH, temperature, and amino acid concentration on cell growth. Cell growth can be assessed in a short time period or by increase of the cell count or size, or by inclusion of radioactive precursors into cellular DNA. These real advantages compared with investigations on intact animals put cell cultures on a par with cultured microorganisms as an experimental system.

When working with cell cultures, we can obtain significant results only on a fairly small number of cells. Experiments requiring 100 rats or 1000 humans for clearing up some matter can be conducted using 100 cultures on cover glasses with equal statistical significance. So if every cell is regarded as an independent object of the experiment, one culture on a cover glass can give an answer as reliable as a clinic full of patients can. This is a significant advantage when it concerns humans; besides, it removes a number of ethical problems from the agenda when it is necessary to use a large group of animals for an experiment.

### 4.2. Cell life cycles

Cell culture monolayers are populations of cells having certain species and tissue origin growing on the surface of a carrier made of plastic, glass etc. A complete cell monolayer may cover more than 90% of the surface, with the cell membranes connected. In such conditions, an average cell size is 20–30  $\mu\text{m}$  at 5.5- $\mu\text{m}$  thickness.

Cell cultures may be roughly divided into two main groups: (1) continuous cultures that are capable of unrestrictedly long existence *in vitro*; (2) diploid ones obtained from normal body tissues retaining many features of the original tissue and capable of restricted (up to 50 divisions) growth in an artificial medium.

In turn, the first group is divided into two subgroups:

(1) high-transformed ones, derived, as a rule, from various tumors and capable of existing in artificial conditions for an uncertain time, (2) low-transformed ones derived from normal

tissues whose transformation source is often unclear, also capable of unrestricted growth but closer to normal body tissues in many respects.

In compliance with the experimental terms, all the three cell culture types were used. The selection of the cultures was chiefly due to by their sensitivity to herpes simplex virus type.

All the cell cultures of the endotherm have similar cell cycle duration—19 to 24 h. The cell cycle consists of the following phases:

1. The presynthetic phase (G1) (phase formula  $2n2c$ , where  $n$  is the chromosome count, and  $c$  is the molecule count in the cell). It starts immediately after the cell division. There is no DNA synthesis yet. The cell actively increases in the dimensions, increases supplies of the substances necessary for division: proteins (histones, structural proteins, and enzymes), RNA, and ATP molecules. Division of mitochondria and chloroplasts (i.e., structures capable of reduplication) occurs. The features of interphase cell organization are being restored after the previous division.
2. The synthetic phase (S) ( $2n4c$ ). The genetic material duplicates by DNA replication. It occurs in a semiconservative way when the DNA double spiral separates into two chains, and a complementary chain is synthesized on each one. This results in the formation of two identical DNA spirals, each one consisting of one old and one new DNA chain. The amount of genetic material doubles. Besides, RNA and protein synthesis continues. A small part of mitochondrial DNA also undergoes replication (most of it replicates in G2 period).
3. The postsynthetic phase (G2) ( $2n4c$ ). DNA is not synthesized anymore, but the synthesis flaws of S period are corrected (reparation). Also, energy and nutrients are accumulated; synthesis of RNA and proteins (mainly nuclear ones) continues.
4. The quiescent phase (G<sub>0</sub>) wherein the cell only consumes the survival minimum of nutrients without preparing for another multiplication cycle.

Each phase is characterized by a different intensity level of nutrient absorption/exchange/release, and these processes can localize in various parts of the cells (the nucleus, cytoplasm, and organelles) depending on the cell cycle phase.

It is also noteworthy that in an actively growing continuous cell culture more than 90% cells enter the cycle, while in a diploid cell culture at most 20% cells (more often less than that) do so.

At a certain cycle phase, the percentage of cells in an actively growing cell culture approximately complies with the phase duration ratio; cells in G<sub>0</sub> phase prevail in a closely packed cell monolayer.

#### 4.3. L41, Vero, and HLE-3 cell lines

In compliance with the passport of L41 CD/84 cell line Ref. [32], a strain of continuous cells G-96 derived from the blood of a patient with monocytic leukemia is known, which was used in 1966 by Solovyov et al. to derive a subline (G-41) specifically resistant to Cocksackie B3 virus by triple treatment with large doses of the virus.

By its morphological features, L41 cell line is an even monolayer of distinct epithelium-like polygonal or roundish cells; there is a constant 4–6% share of giant cells. The cytoplasm is fine-granular. The nuclei are roundish and contain 2–4 nucleoli. There are up to 6% abnormal mitosis forms. The share of cells with irregularly shaped nuclei is 8%. The monolayer was generated on day 3–5 from planting into a medium consisting of equal parts of Eagle medium and 199 medium with 10% bovine embryo serum. The cell maintenance medium contains necessary amino acids, salts, and glucose.

The culture is highly sensitive to poliomyelitis, Coxsackie B, ECHO-19, human adenovirus, and measles viruses.

Vero cell line was derived from normal simian renal cells (those of an adult African green monkey). The number of generations and passages: over 120 passages before the test start. The line has been used in a laboratory research since 1962. The monolayer forms on days 3–5 from the planting moment. The multiplying factor is 6–7 on day 5.

The morphological features: epithelium-like cells, polygonal, with notable vacuolization, and distinctly oriented growth zones.

The karyological characteristics: the cells correspond to the monkey karyotype by their structure—44 diploid cells, 3 hyperploid cells, and 53% hypoploid cells.

Species origin: monkey, confirmed karyologically. Data on contamination: no bacteria, fungi, or *Mycoplasma* detected. The cell line is maintained in the growth medium + 10% glycerin in liquid nitrogen. About 80–85% cells restore on defrosting. The culture is highly sensitive to poliomyelitis viruses and arboviruses.

HLE-3 cell line was derived by Yekaterinburg Institute of Viral Infections (YRIVI) staff from normal human lung tissue. The technique for obtaining this cell line was developed in the cell line laboratory of YRIVI by Glinskikh et al. in 1980 from the lung of a 12-week human embryo from a healthy female whose genology was free from malignant or hereditary diseases.

The number of generations and passages: 20 passages at most before the test start.

The monolayer forms on days 4 and 5 from the planting moment. The morphological features: fibroblastic cells with distinct edges.

The karyological characteristics: the cells correspond to the human karyotype by their structure. The modal class contains 87% cells with normal diploid human chromosome set.

Species origin: human, confirmed karyologically with an isoenzyme technique.

Data on contamination: no bacteria, fungi, or *Mycoplasma* detected. The cell line is maintained in the growth medium +10% glycerin in liquid nitrogen. About 70% of the cells restore on defrosting.

Sensitivity to viruses: the culture is highly sensitive to polioviruses 1, 2, and 3, Coxsackie B3, BARinsECHO 3, 6, 11, 13, 19, 20, 24, 28, RS viruses, and herpes simplex virus.

## 5. Procedure and technique of experimental research

We used the theory presented in Section 3 to study the processes occurring in a thin layer of live cells. In the text below, a description of the experiment, its errors, and the measurement calibration is given. The latter procedure by default stemmed from the experiment conducted to check one of the tenants of the theory.

### 5.1. Thermostats and temperature control

Precise maintenance of the temperature in the medium for the cells plays an important role in the experiments. After several attempts to create a small thermal chamber to maintain the temperature in the small region, we decided on placing the entire optical system into a thermostat of suitable dimensions. We used three thermostats: (a) a self-made laboratory thermostat, (b) a liquid thermostat of 3LI-1125M type, and (c) an air bath of TCЭ-200 type.

We used the laboratory thermostat in the cases when we had to place the substrate with cells in a horizontal position. The photo of the thermostat is shown in **Figure 3**.



**Figure 3.** Photograph of laboratory thermostat.

We used a dustproof chamber of a scanning atomic-force microscope. To heat the air inside the chamber, we used a liquid ultrathermostat U10 connected to the radiator with pipes which is common for Russia. The radiator was in the lower part of the chamber under the table for the microscope: it was blown over by six small ventilators. A metallographic microscope of Axio 40 MAT type that we used to generate speckle images of the cells was placed on the table.

The temperature of the cuvette in all the thermostats was determined by a temperature sensor of DS18B20 type of precision to  $\pm 0.1^\circ\text{C}$ . The signals from the sensor entered the computer; the temperature values were displayed in the monitor or recorded into the computer memory in the preset time.

The laboratory thermostat maintained the temperature of the cuvette to  $\pm 0.1^\circ\text{C}$  precision for several hours, and the liquid thermostat 3LI-1125M did so for several days. An air bath was used to study the cell reaction to temperature.

## 5.2. Optical and television systems

When the laboratory thermostat was used, the transparent substrate with cells was placed at the bottom of a special cuvette. In turn, the cuvette was placed on the stage of the microscope. The transparent lid of the cuvette was placed so that (1) the nutrient solution about 1 mm thick was placed above the cells and (2) there was no free liquid surface. Above the lid, there was matte glass that was illuminated by a diverging beam from the semiconductor laser module. The speckle image of the cells was entered into the computer using a monochrome TV camera of Videoscan—415/P/C-USB type. The camera had a photosensor array of  $6.5 \times 4.8$  mm size with  $780 \times 572$  cells (pixels) of  $8.3 \times 8.3$   $\mu\text{m}$  size. The frame input frequency was up to 25 Hz. The signals from the TV camera entered the laptop computer of Aspire 3692 WLMi 8 type by Acer firm via a USB port. A semiconductor laser module of KLM-D532-20-5 type with wavelength  $\lambda = 0.532$   $\mu\text{m}$  and 20 mW power was used as the light source. Note that the above TV camera and laser were used in all of our optical systems.

In the liquid thermostat and in the air bath, optical systems with the upright position of the substrate with cells in the optical cuvette were used. The logic chart of the optical systems is given in **Figure 4**, and its photograph is presented in **Figure 5**.

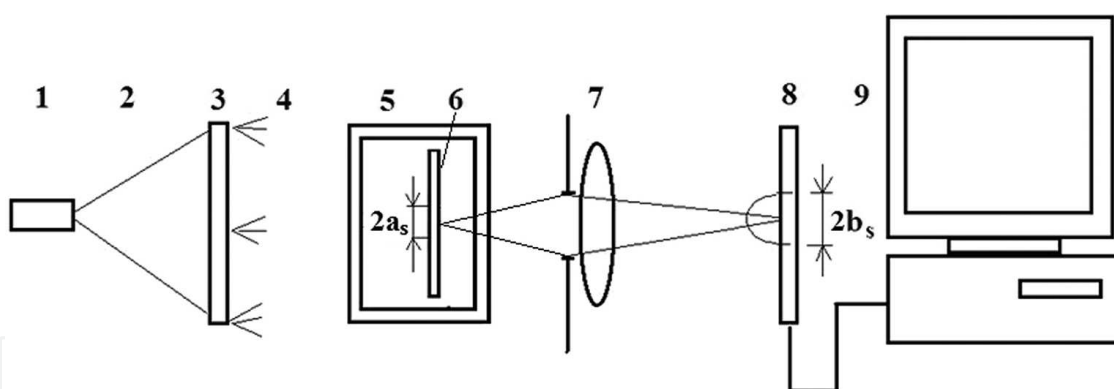


**Figure 4.** Logic chart of optical device: (1) laser module, (2) illuminating beam, (3) matte glass, (4) scattered radiation, (5) cuvette, (6) substrate with cells, (7) lens with diagram, (8) photosensor array, (9) computer.

## 5.3. Software

Input of the image frames into the computer was made using the software coming standard with camera Videoscan—415/P/C-USB. The frames entered into the computer were processed to obtain dependences  $\eta(t)$  and  $\tilde{I}(t)$  using two original computer programs. The first program was intended to process the frames already entered into the computer. The operator displayed the first frame of the speckle image onto the monitor and selected the fragment of the frame to determine  $\eta$  using the mouse or the keyboard. Then it gave the second frame or a mass of frames. In the first case, the program displayed value  $\eta$  using Eq. (34) and digital value  $\tilde{I}$ , in the second case, it displayed dependences  $\eta(t)$  and  $\tilde{I}(t)$  onto the monitor. The first program also



allowed to obtain the distribution of values  $\eta$ . The operator selected two frames corresponding to time moments  $t_1$  and  $t_2$ . Then the operator selected a segment on the displayed image and divided it into subsegments. The program digitized the fragment and determined value  $\eta$  in every subsegment using Eq. (34). The obtained values were recorded into the computer memory as a matrix in text format to be processed.

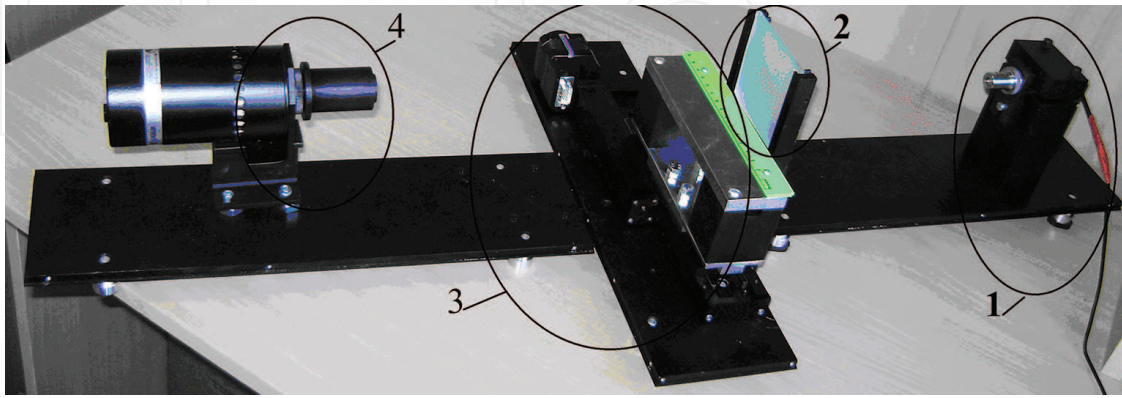


**Figure 5.** Photography of the optical device: (1) laser module with microobjective, (2) matte glass, (3) lock of the object on the platform of the motorized translator, (4) camera with lens.

Value  $\eta$  was determined by Eq. (34):

$$\eta = \frac{\frac{1}{m \times n} \sum_{i=0}^{m-1} \sum_{j=0}^{n-1} [A_{i,j} - \bar{A}][B_{i,j} - \bar{B}]}{\sqrt{\frac{1}{m \times n} \sum_{i=0}^{m-1} \sum_{j=0}^{n-1} [A_{i,j} - \bar{A}]^2} \times \sqrt{\frac{1}{m \times n} \sum_{i=0}^{m-1} \sum_{j=0}^{n-1} [B_{i,j} - \bar{B}]^2}}, \quad (34)$$

where  $A_{i,j}$  are digitized signals at a segment of  $m \times n$ -pixel size at initial time point  $t_1$ ,  $B_{i,j}$  are the signals in the same segment at a different time point  $t_2$ ,  $i$ , and  $j$  are the segment pixel numbers  $xd$  and  $yd$ , respectively,  $\bar{A}$  is the mean signal value in the segment at the start time, and  $\bar{B}$  is the mean signal value in the segment at time moment  $t_2$ .

The second program in DOS medium permitted real-time determination of digital values  $\eta$  and  $\tilde{I}$ . First, the operator set  $x$  and  $y$  coordinates of the pixels (up to 40 pieces) on the program interface. By the operator's command, the program determined digital values of mean intensity  $\tilde{I}$  in the above pixels, and it obtained  $\eta$  values in the neighborhood of the pixels using Eq. (34). Masses  $\eta$  and  $\tilde{I}$  were saved in *txt* format in preset files. The program could work for several days continuously.

#### 5.4. Errors and calibration of optical measurements

We assessed the error of value  $\eta$  determination by Eq. (34). In compliance with the indirect measurement error assessment techniques recommended in Russia [31], the mean square deviation of random error  $S(\tilde{\eta})$  in the indirect measurement result is determined by Eq. (35):



$$S(\tilde{\eta}) = \sqrt{\sum_i^m \left( \frac{\partial \eta}{\partial a_i} \right)^2 \times S^2(\tilde{a}_i)}, \quad (35)$$

where  $\tilde{\eta}$  is experimentally found value of  $\eta$ ,  $a_i (i = 1, \dots, m)$  are values  $A_{i,j}$  and  $B_{i,j}$  featuring Eq. (34),  $\frac{\partial \eta}{\partial a_i}$  is the first derivative of function  $\eta$  by argument  $a_i$ , calculated at point  $\tilde{a}_1, \dots, \tilde{a}_m$ ,  $\tilde{a}_i$  is the result of measuring value  $a_i$ , and  $S(\tilde{a}_i)$  the mean square deviation of random errors in the result of measuring the  $a_i$ -th argument.

We performed the transformations by Eq. (35) and assessed the error of value  $\eta$  determination in a typical experiment. We selected the variant with 8-bit digitization of the radiation intensity averaging-out half the dynamic range, the minimum speckle size slightly exceeding the TV camera pixel size, and  $S(\tilde{a}_i) = 0.7$ . Calculations showed that value  $\partial \eta / \partial a_i$  featuring Eq. (35) consists of sum  $m$  of random  $10^{-2}$ -order values of different signs. The random sign value appears due to randomness of intensity deviation from the average value in the speckle field. In the model experiment, a reflecting rough object in the form of a metal plate was used, and value  $\eta$  varied due to its shift. For a  $10 \times 10$ -pixel fragment of the speckle image, we obtained that  $S(\tilde{\eta})$  decreases steadily with increase of  $\eta$  in the range from 0.3 to 0.999, and the relative error of  $\eta$  determination does not exceed 1%.

Essentially, the calibration technique for the optical systems intended to determine the optical path dispersion value was developed in Ref. [29]. In this technique, batched random variations of the wave phase difference were set by means of shifting a 1-mm thick transparent plate. The plate shift  $u_x$  was performed with a  $0.12\text{-}\mu\text{m}$  pitch. The plate roughness was prechecked with a WYKO NT-1100 optical profilometre. **Figure 6** shows experimental and theoretical dependences of  $\eta$  on the plate shift  $u_x$ .

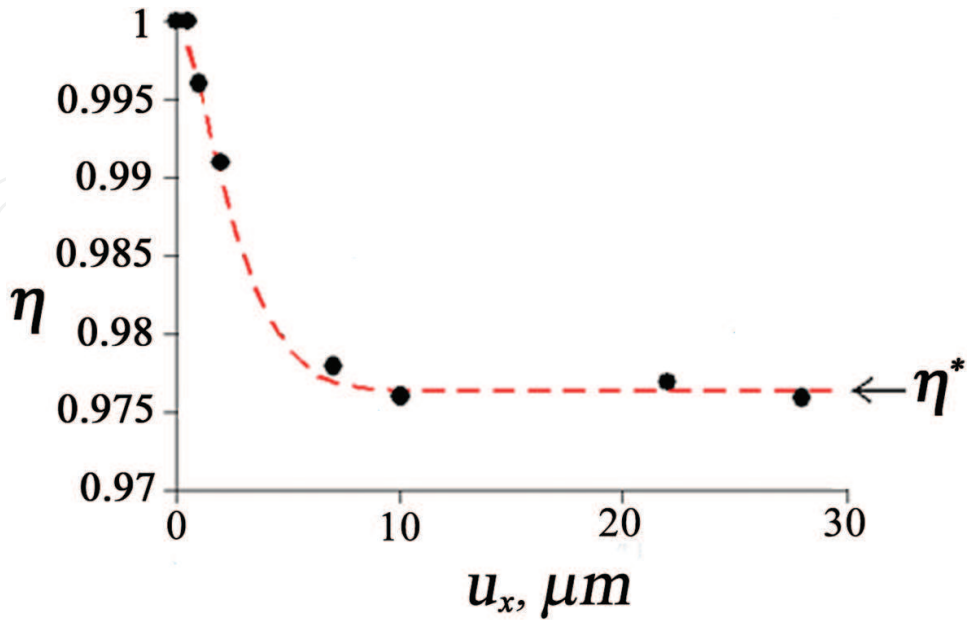


**Figure 6.** Theoretical (---) and experimental dependences  $\eta(u_x)$ .

As is seen from the graphs, when the plate is shifted for a value exceeding the characteristic surface roughness size, the correlation coefficient levels off to  $\eta^*$ . The theoretical curve was obtained for the Gaussian function by Eq. (27). The difference between the theory and the experiment was in the range of 2.5%. Roughness parameter difference  $R_a$  obtained by level  $\eta^*$  from that measured by the profilometre was in the range of 5%. The experiment details and the digital derivations can be found in Ref. [29]. This experimental technique can be used to calibrate the equipment used to determine value  $k_{22}$ . As for the calibration of the device for determination of value  $\langle x_2 \rangle$ , further research is needed to perform this procedure.

Good coincidence of the data obtained by the speckle dynamics and with the optical profilometre (**Figure 6**) is to a great extent determined by small errors of determining the speckle image correlation coefficient  $\eta$  and with high sensitivity of the technique. Let us assess the sensitivity limits of the equipment for the determination of values  $\langle x_2 \rangle$  and  $\sigma_u$ . Let us admit that in Eq. (26) values  $\langle x_1 \rangle$ ,  $k_{11}$ ,  $k_{22}$ , and  $k_{12}$  are equal to zero. Typical values  $\eta_{12}$  equaled 0.99 in the absence of the object. Then for wavelength  $\lambda = 0.532 \text{ } \mu\text{m}$ , we obtain that  $\Delta u = (\lambda/2\pi)\arccos 0.99 = 12 \text{ nm}$ . Hence, it follows that the limit sensitivity of the device related to the optical path difference generated in the range of the linear resolution of the lens equals 12 nm. Let us admit that the object thickness is invariable, and the optical paths vary due to variation of the mean refraction index. For instance, for the 10- $\mu\text{m}$  cell thickness, we obtain that the refraction index will vary by  $1.2 \times 10^{-3}$ . Now let us find the limit sensitivity of the equipment in determination of mean square deviation  $\sigma = [\lambda/(2\pi)]\sqrt{k_{11}}$  of value  $\Delta u$  by value  $\eta^*$ . Supposing again in formula  $\eta^* = \exp(-k_{11})$  that  $\eta^* = 0.99$ , and  $\lambda = 0.532 \text{ } \mu\text{m}$ , we obtain that  $\sigma = [\lambda/(2\pi)]\sqrt{-\ln 0.99} = 8 \text{ nm}$ .

It is noteworthy that values  $\eta_{12}$  and  $\eta^*$  equal to 0.99 appeared due to application of medium-quality equipment. If limit values  $\eta_{12}$  and  $\eta^*$  equal to 0.999 are reached due to noise decrease, then the sensitivity to the mean value and dispersion of value  $\Delta u$  will equal 4 and 3 nm, respectively.

## 6. Experiments

### 6.1. Studying speckle dynamics in the image plane of a cultured cell monolayer

We studied the features of speckle dynamics caused by an activity of cultured cells on L41 cells discussed above in Section 4.3. After the formation of a monolayer, the substrate with the cells was placed into an optical cuvette filled with nutrient solution. A cell-free substrate of similar thickness was placed near. Next, the cuvette was fixated on the optical device shown in **Figure 5** that was placed in liquid thermostat 3LI-1125M. The typical magnification by the optical system was 0.25, and the typical linear resolution of the lens was 60  $\mu\text{m}$ .

**Figure 7** presents a typical speckle pattern recorded in the image plane of the cuvette with substrates.

After equalization of the temperatures of the cuvette and the thermostat the mechanical system was checked for stability. To do so, we used the above software, selected the segment of the

frame near the image of the cuvettes. Using two speckle images of the segment recorded in 1 or 2 min, we determined the value of correlation coefficient  $\eta$  of their digital images. If value  $\eta$  equalled 0.99 or 0.98, the system was considered mechanically stable. Further, we recorded the film of the speckle dynamics lasting 20–40 s with 25 Hz frequency. Using the software discussed in Section 5.3, we obtained dependences of the speckle image fragment correlation coefficient  $\eta$  on the time using the frames of the film. In **Figure 7**, typical selected fragments are shown by white frames.

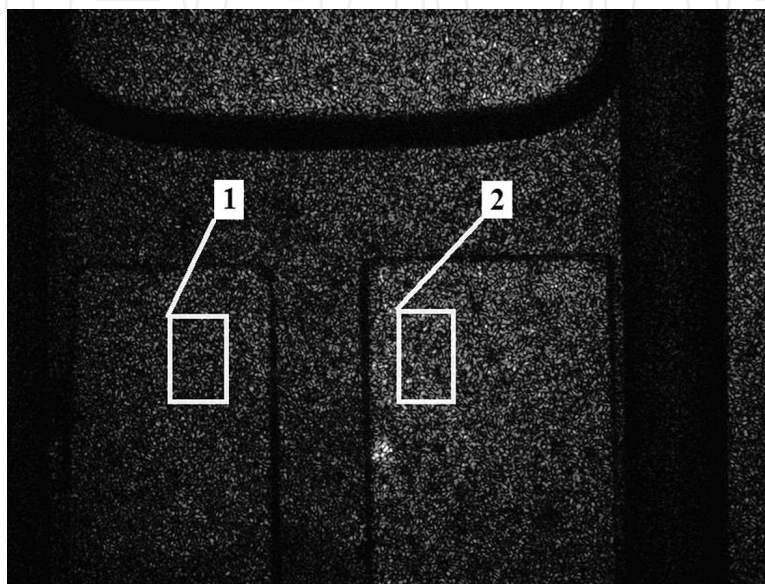


**Figure 7.** Typical speckle image of a cuvette with transparent substrates: the substrate with cells is on the left, and the cell-free one is on the right. The selected image fragments are denoted by numbers.

**Figure 8** shows typical dependences of  $\eta(\tau)$  for the cells in the nutrient solution (dependence 1) and for the nutrient solution (dependence 2) obtained after processing of the film. The dotted lines show theoretical dependences obtained using Eq. (27) for normalized Lorentzian function  $k_{12}(\tau)$ . Analysis of the experimental dependences obtained in different segments of the substrate with cells within its image showed that the deviation of the theory from the experiment was in the range of 8–11%.

As seen from the graphs in **Figure 8**, in about 5 s dependences  $\eta(\tau)$  level off. The mean square deviation of the last four points from their mean value does not exceed 1%. In compliance with the theory discussed above in Section 3, levelling off dependence  $\eta(\tau)$  means that random process  $\Delta u = \Delta u(t)$  is stationary in time. Value  $\Delta u$  is typical (mean) optical wave path difference within the region with cells of 60- $\mu\text{m}$  diameter. As fragments of about 1-mm size correspond to the selected segments of the speckle images in the object plane (**Figure 7**), random process  $\Delta u = \Delta u(t)$  can also be regarded as homogeneous in this fragment.

As was pointed out in Section 3, by values of variable  $\eta = \eta^*$  we can determine the corresponding dispersions of the wave pair optical paths  $\sigma_1^2$  and  $\sigma_2^2$  in the horizontal segment of dependences 1 and 2. Supposing that optical wave path variations in the cells and in the

nutrient solution are uncorrelated, we can show that the optical path dispersion in cells can be determined using Eq. (36):

$$\sigma_u^2 = \sigma_1^2 - \sigma_2^2. \quad (36)$$

Mean square deviation  $\sigma_u$  of values  $\Delta u$  obtained by Eq. (36) came to 14 nm.

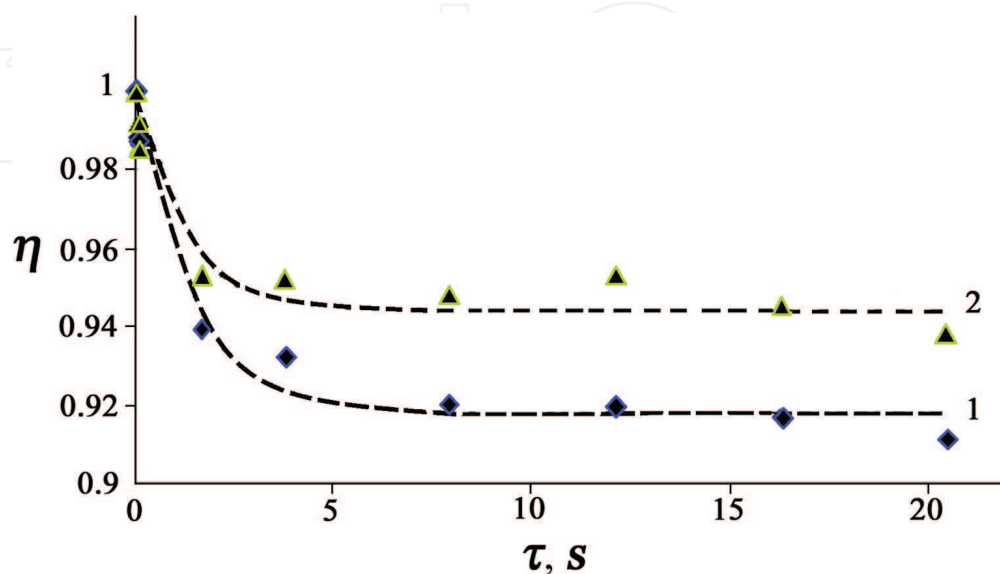


**Figure 8.** Joint dependences of  $\eta$  on the time for the cells in the nutrient solution (1) and for the nutrient solution (2).

The homogeneity and stationarity of process  $\Delta u = \Delta u(t)$  in a segment of a 1-mm order can be explained by the fact that in a monolayer, the cells are closely packed, so there is no variation of their shape due to translation and division. In these conditions local deviations of the medium refraction index from its mean value are possible at the structural level. As was discussed above in Section 3, chemical reactions and phenomena of mass transfer can be the reasons for refraction index variation.

## 6.2. Defrosted cells and speckle dynamics

We conducted an experiment with L41 cells precipitated onto a transparent substrate immediately after defrosting. The interest in similar experiment was caused by the fact that, as distinct from a monolayer of cultured cells, after defrosting the cells do not attach to the substrate immediately, being in motion. When a cell is moved for a distance comparable to its size, the sounding wave pair path difference can vary by a value comparable to wavelength of radiation  $\lambda$  and exceeding it. Therefore, in compliance with Eq. (26) variation of speckle image fragment correlation coefficient can be caused both by the cosine argument variation and by variation of the values in the exponent. As a cosine can be both positive and negative, appearance of negative values of the variable close to 1 would speak for correctness of Eq. (26) and our theory.

Besides, the objective of the conducted research was to study the possibility to apply the technique at large magnifications to analyze the processes occurring in different parts of one cell.



The experiments were conducted on a laboratory device with a horizontal position of the substrate with cells. When the temperature reached the value near  $36^{\circ}\text{C}$  a glass 0.1-mm thick was placed into a cuvette with nutrient solution, and poured frozen cells from Dewar vessel onto it. After the temperature stabilization in 30–60 min, recording of the speckle dynamics film was started. The optical magnification was about  $\times 8$ , the exposure time equaled 9 s, and the frames were recorded for several hours.

A typical speckle pattern of cells precipitated on a substrate is shown in **Figure 9**. Viewing of the films showed that the cells contact other cells being in continuous random motion. The typical shift of a cell in one direction was comparable to its dimensions. There were cells making shifts for a larger distance, and there were also cells that could be visually regarded as stationary.

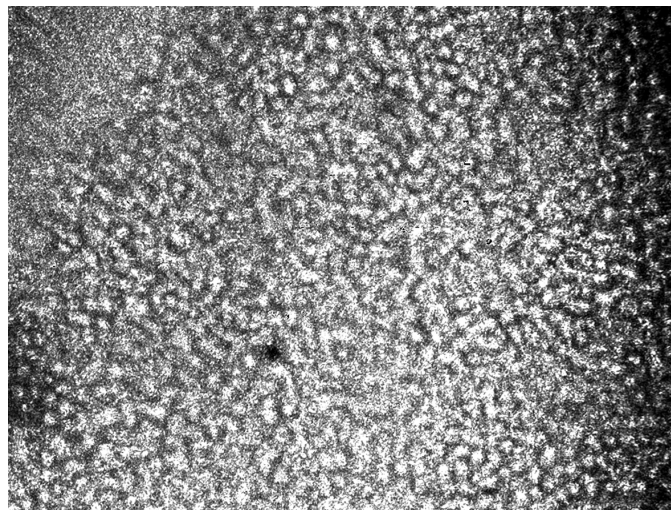


**Figure 9.** Speckle image of defrosted cells.

**Figures 10–13** demonstrate typical dependences  $\eta = \eta(\tau)$  obtained for different sizes of speckle image segments. The graph in **Figure 10** corresponded to a  $4 \times 4$ -pixel segment or the cell fragment size of about  $4 \times 4 \mu\text{m}$ . Originally, the segment was in the center of the cell image. The rest of the dependences were obtained by means of data averaging in segments containing from 4 to 200 cells.

As seen from **Figure 10**, for a randomly moving cell value  $\eta$  randomly varies in the range from -1 to +1 around zero. The obtained result qualitatively confirms correctness of Eq. (26) containing dependence of value  $\eta$  on the optical wave path difference by the cosine law. Variation of  $\eta$  from 1 to -1 means that the positive image has changed to a negative one, or vice versa. This is possible, for example, if in all the 16 pixels radiation intensity varies by the cosine law with the same period (the same  $\Delta u$ ) but with the different initial phase. In **Figure 10**, value  $\eta$  does not reach +1 and -1 again. It points out that either during the cell motion its shape changing in a  $4 \times 4 \mu\text{m}$  segment is inhomogeneous, or value  $\eta$  varies not only by the cosine law.

If the data averaging region covers plenty of cells (see **Figures 11–13**), values of variable  $\eta$  are positive and reach a horizontal segment in about 0.5 h. The obtained data can be explained by the fact that at a fixed time point values  $x$  included in the cosine argument in Eq. (26) can reach large values with different signs in different cells. But in averaging by a large count of cells (the

objects of the ensemble) variables  $\langle x_1 \rangle$  and  $\langle x_2 \rangle$  have values close to zero. Then in Eqs. (26) and (31) the dependence on the cosine disappears, but the dependence on  $k_{22}$  remains.

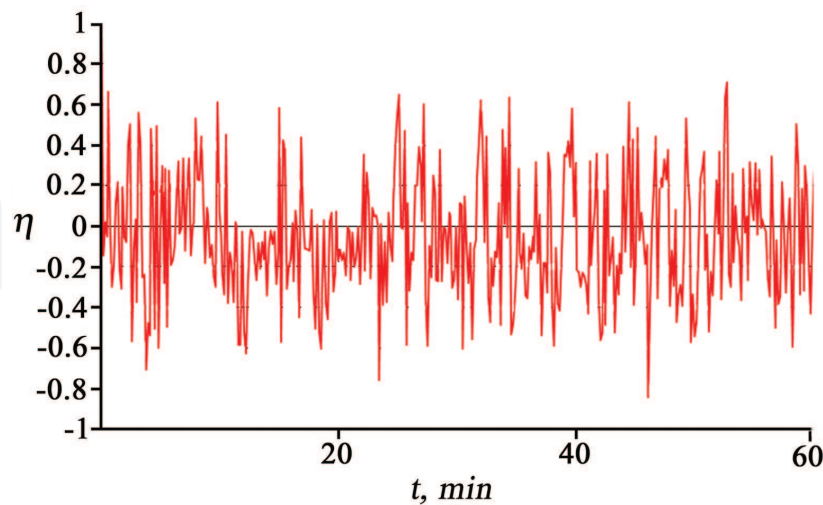


**Figure 10.** Dependence  $\eta = \eta(t)$  for fragment inside the cell image.

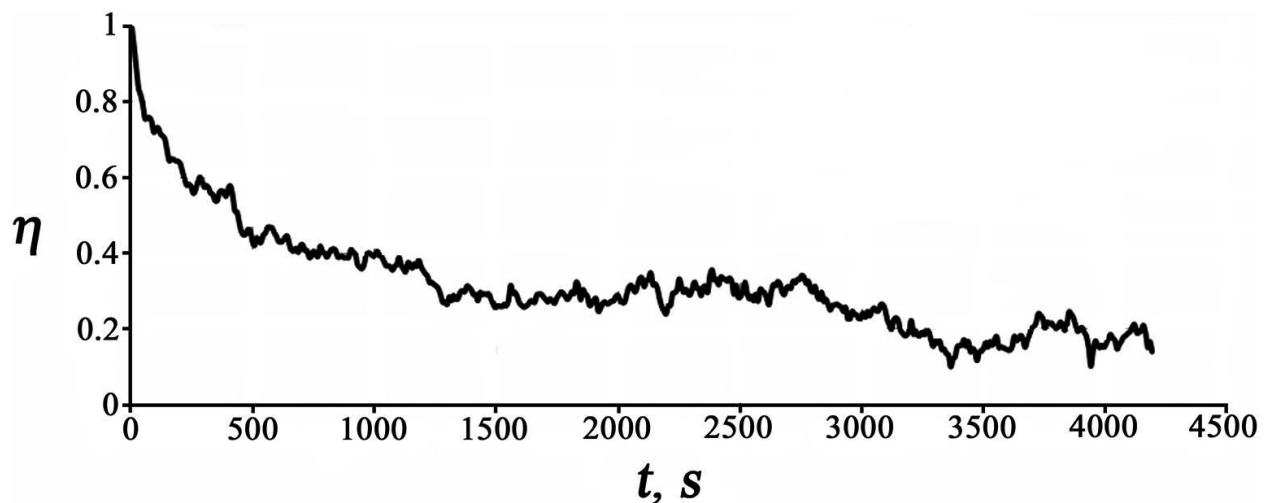


**Figure 11.** Dependence  $\eta = \eta(t)$  corresponding to four cells.

Dependences  $\eta(t)$  shown in **Figures 11–13** can be interpreted in two ways. Supposing that the 9-s speckle averaging time exceeds the correlation time of the fastest processes in the cells, one can suppose that by Eq. (31) dependence  $\eta(t)$  corresponds to an unstable process wherein value  $k_{22}$  first increases continuously and then levels off. On the other hand, we can suppose that graphs of  $\eta(t)$  correspond to stationary process  $\Delta u(t)$  with the correlation time about 30 min.

To clear up this matter, we selected different segments of the view-field containing about 100 cells. For each of these segments, four dependences  $\eta(t)$  lasting about 1 h were built for different time intervals. The form of dependences was well reproducible, the multiple correlation coefficients of the four masses was in the range from 0.86 to 0.96. We came to the conclusion that in fragments containing hundreds of defrosted cells random processes  $\Delta u(t)$  can be regarded as homogeneous in space and stationary in time for several hours.



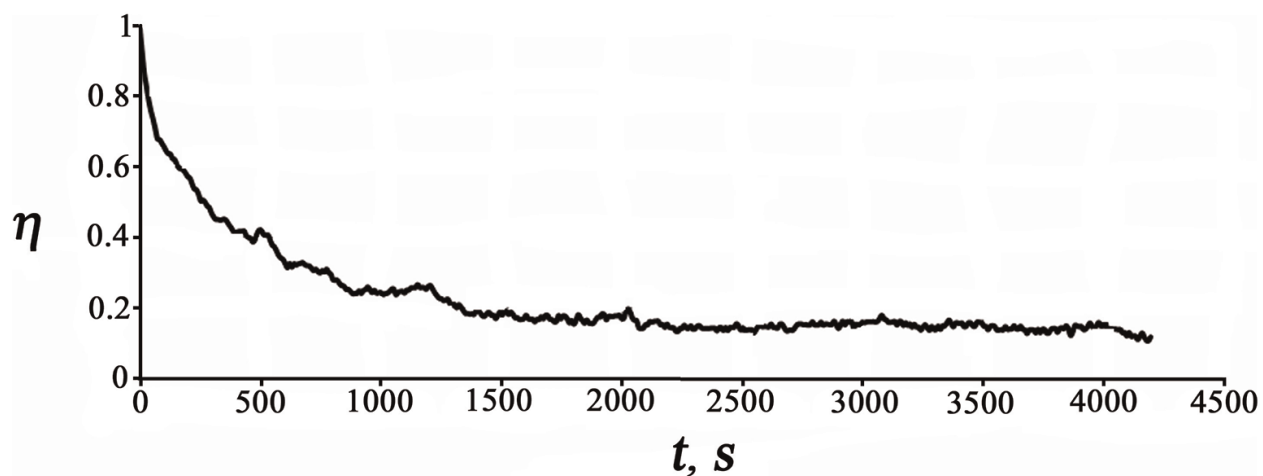


Figure 12. Dependence  $\eta = \eta(t)$  corresponding to 60 cells.

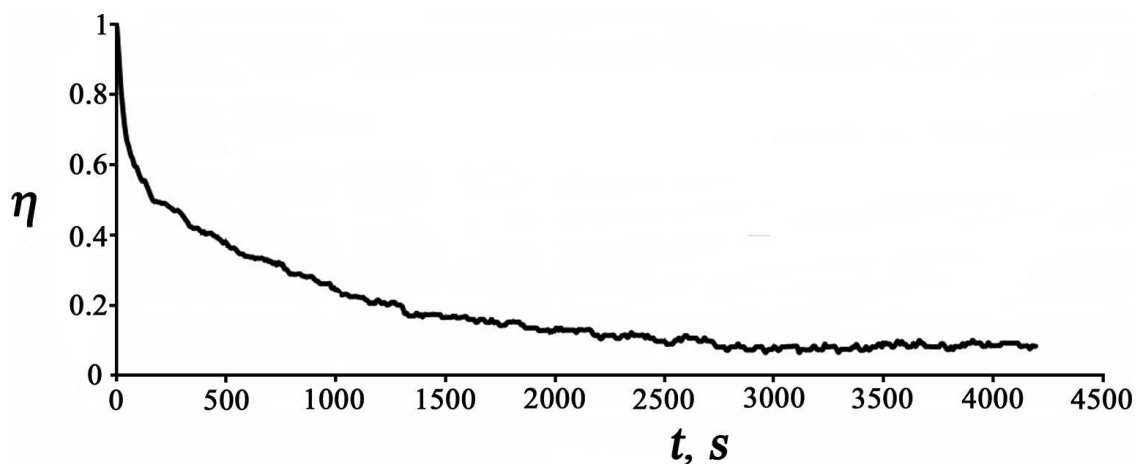
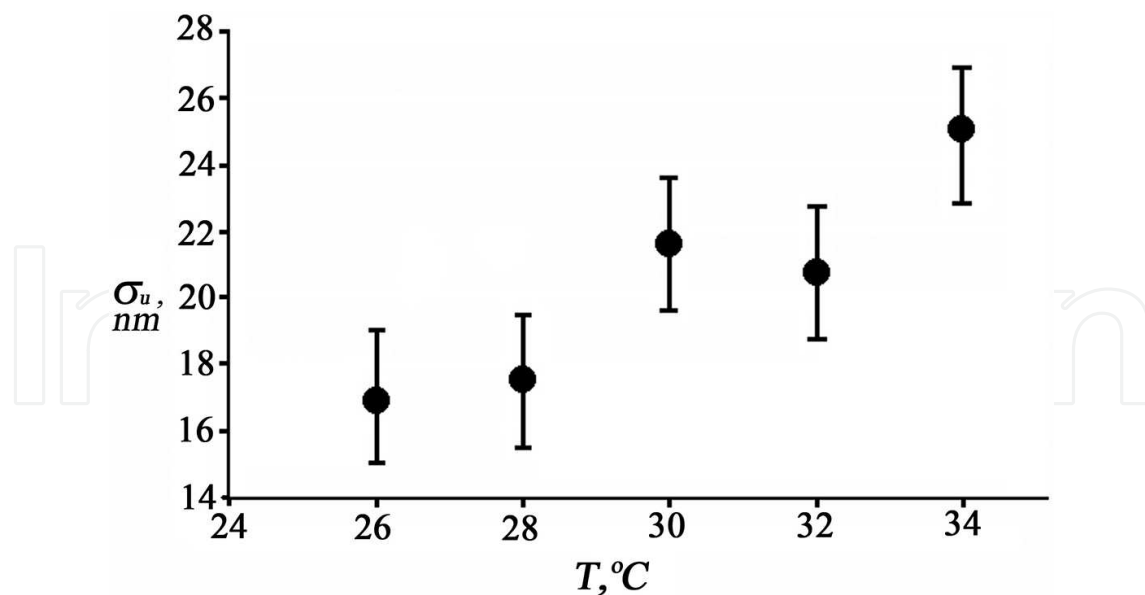


Figure 13. Dependence  $\eta = \eta(t)$  corresponding to 200 cells.

### 6.3. Application of speckle dynamics for studying the reaction of a cell mass and fragments of individual cells to temperature variations

The theoretically detected and experimentally confirmed relation between the correlation coefficient of speckle images  $\eta$  and the dispersion of the optical wave pair path difference  $\sigma_u^2$  was immediately used in our first experiments studying dependence of  $\sigma_u$  on temperature  $T$ . The details of the experiment can be found in Ref. [33]. A segment of L41 cell monolayer containing hundreds of cells was the averaging region. Value  $\sigma_u^2$  corresponding to the cells was obtained as the difference of values  $\sigma_u^2$  corresponding to the cells in the nutrient solution and to the nutrient solution. The cuvette with cells was first heated to a temperature around 40°C. Then the heating was stopped, and when the cuvette cooled to room temperature, speckle dynamics films lasting 20–40 s were recorded with 25-Hz frame rate. The optical system presented in **Figure 5** was used. **Figure 14** presents dependence of  $\sigma_u$  on temperature  $T$  obtained experimentally. As seen from the given graph, an approximately linear relation between  $\sigma_u$  and  $T$  is found.



**Figure 14.** Dependence of  $\sigma_u$  on  $T$  for L41 cells.

The purpose of the next experiment was studying the reaction of small fragments inside a cell and a small group of cells to temperature variation. As distinct from the previous experiment, the frames were recorded continuously with heating of the thermostat from the room temperature to 43°C in about 2 h. The averaging time (the frame exposure time) equaled 9 s. We used an air bath of TCЭ-200 type and an optical system with an upright position of the substrate. An L41 cell monolayer was the research objective. For the experiment, we selected a segment that contained at least a small cell-free area (**Figure 15**) in the view-field. The magnification was  $\times 8$ , and about 10–30 pixels of the TV camera matrix fell onto an image of an individual cell.

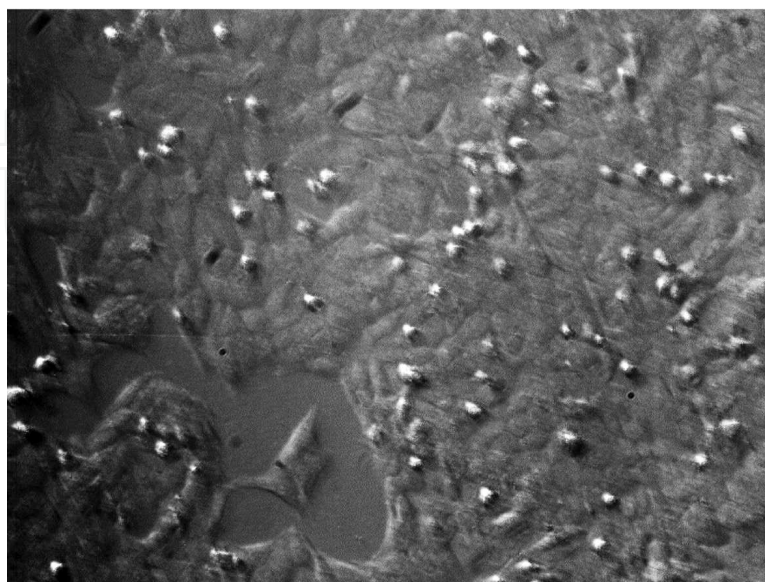


**Figure 15.** Photographs of cells in white light. A cell-free fragment is visible in the lower part of the frame.

Next in **Figure 16**, there is distribution of value  $\eta$  obtained at the temperature of 30°C by 2 speckle cell images shown in **Figure 15**. The time interval between the frames equaled 18 s. Values  $\eta$  were found in segments of  $10 \times 10$ -pixel size.

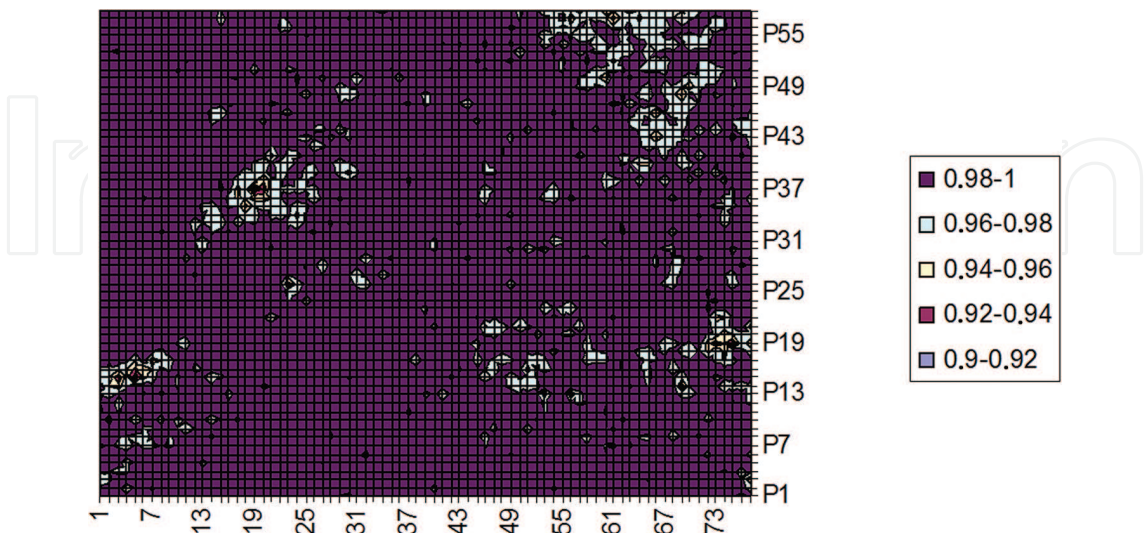


**Figure 16.** Distribution of value  $\eta$  obtained by two speckle images.

**Figures 17, 18 and 19** show typical dependence  $\sigma_u$  on temperature and joint dependences of  $\sigma_u$  and temperature  $T$  on time. Value  $\sigma_u$  was obtained using two dependences  $\eta(t)$  corresponding to the cells in the nutrient solution and to the nutrient solution. Segments containing 60 cells (**Figure 18**) and small regions inside the cells were averaging regions (**Figure 17**). As is seen from the pictures, considerable fluctuations of  $\sigma_u$  are observed with temperature increase. Fluctuations of value  $\sigma_u$  differ from one cell part to another. If the temperature gets stabilized in 30 min,  $\sigma_u$  also stabilizes (**Figure 19**). The correlation coefficient of masses  $\sigma_u$  and  $T$  shown in **Figure 19** equals 0.88.

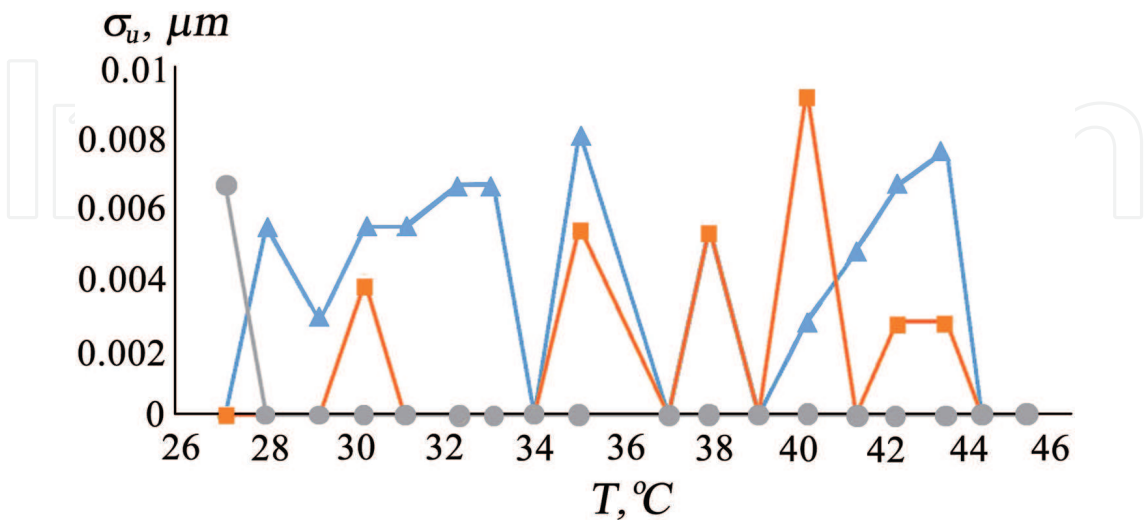


**Figure 17.** Dependences of  $\sigma_u$  on  $T$  for three segments inside one cell. Red colour – cell edge, gray colour – cytoplasm, blue – cell center.

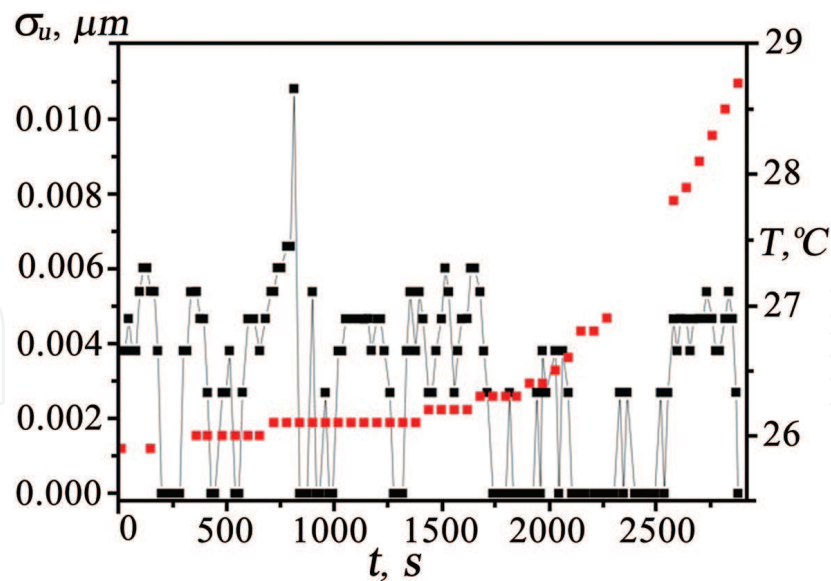


**Figure 18.** Joint dependences  $\sigma_u$  on time and those of temperature on time.

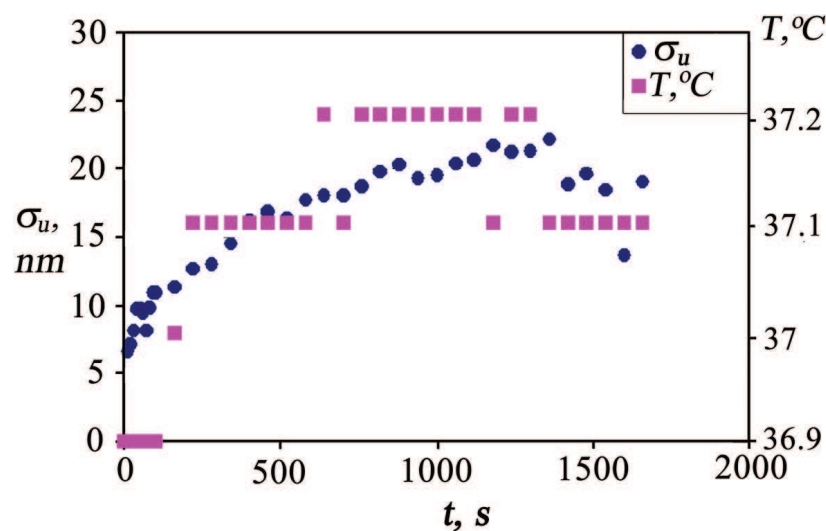


**Figure 19.** Joint dependences  $\sigma_u$  and temperature on time at small heating rates.

So on the basis of the conducted research, we can conclude that with temperature increase from 25° to 43°C at the rate of about 0.5° a minute, there are fluctuations of value  $\sigma_u$  in space and time. With decreasing variation rate of temperature  $T$  by an order variations of  $\sigma_u$  stabilize, and the dependence of  $\sigma_u$  on  $T$  becomes linear. To study the dependence of  $\sigma_u$  on  $T$  in small segments inside the cells in detail, further research is needed.

#### 6.4. Comparison of theory and experiment: cell activity parameters

Our experiments on cultured and defrosted cells showed qualitative coincidence of theory and experiment. So in random cell motions on the bases of a 1- $\mu\text{m}$  order, the mean difference in the optical paths of two waves can reach and exceed wavelength  $\lambda$ . Then, in compliance with the



theory, the value of the cosine and also value  $\eta$  must accept not only positive but also negative values in a random way. Experimental confirmation of this supposition speaks for correctness of the model applied and the calculations made.

We detected good correlation of dependences  $\eta(t)$  corresponding to hundreds of defrosted cells obtained in different time intervals. Absence of dependence of a random process on selection of the counting origin means its stationarity. According to the theory, levelling off dependence  $\eta(t)$  speaks for stationarity of processes  $\tilde{I}(t)$  and  $\Delta u(t)$ . Homogeneity and stationarity of the intracellular processes in defrosted cells detected using two methods can find practical application. In particular, studying the reaction of hundreds of defrosted cells to the effect of viruses, bacteria, and searching the optimum drugs that prevent their development can be promising. Cultured cells can serve this purpose as well. The advantage of cultured cells is their immobility. That is why above-noted studies can be conducted on a small cell number and on individual cells. The advantage to application of defrosted cells is simplicity of the research target preparation.

At present we suggest that it is value  $\sigma_u$ , or mean square deviation of wave pair optical paths obtained by way of averaging by some region that can be regarded as a cell activity parameter.

This selection is well substantiated from the viewpoint of physics. Indeed, if some processes do not occur in the cells, there is no optical path variation, so  $\sigma_u = 0$ . If the processes connected with small energy absorption or emission and with transfer of small amounts of substances arise in the cells, small random deviations of the refraction index and the cell shape from the mean value appear. Therefore, values  $\sigma_u$  will be small as well. With intensification of physical-chemical processes in the cells, the values of  $\sigma_u$  will increase.

The selection of parameter  $\sigma_u$  is justified from the viewpoint of biophysics as well. It is known that at room temperature, the metabolic processes in cultured cells are weakly manifested. The culture techniques have shown that with increase of temperature  $T$ , the metabolic processes become more distinctly manifested and reach their maximum at 34–37°C. The increase of value  $\sigma_u$  with increase of  $T$  (**Figure 14**) in a relatively wide range for hundreds of cells and good linear correlation between  $\sigma_u$  and  $T$  in the range of 0.4°C (**Figure 19**) for tens of cells speaks good reason behind applying  $\sigma_u$  as a cell activity parameter.

That said, it is not clear yet what constituents of cell metabolism affect  $\sigma_u$ . Further, research is needed to clarify the matter.

## 7. Rapid speckle control of cell reaction to herpes simplex virus

The previous sections discussed the theoretical and experimental research that allowed for substantiating the application of speckle dynamics for studies of a thin cell layer activity. This section presents the research results aimed at the study of opportunities for application of the speckle technique for detection of viruses in cells and, in perspective, for therapeutic drug management. The features of speckle dynamics generated by the effect of herpes simplex virus on a monolayer of cultured cells were studied as the first step toward this goal. Initially, it was

necessary to understand if the technique can distinguish between the processes in virus-free and virus-infected cells.

### 7.1. Features of virus development in the cell

Herpes (from Greek herpes—fever) is a viral infection remaining long in the body, predominantly in a latent form Ref. [34]. The most reliable data on herpes were obtained after the virus of this disease was isolated. W. Grüter (1912) first observed development of keratoconjunctivitis in rabbits after administration of the liquid from a human herpetic blister into the scarified sclera. Later, the author made effective successive passages of the viruses on the rabbit eye cornea.

Due to using the negative drug contrasting technique, it was discovered that the external envelope of HSV-1 virus (capsid) has a cubic symmetry type and is an icosahedron. The capsomers composing the capsid are hollow bodies, penta- and hexagonal in the cross-section. Typical viral particles (virions) consist of three main components: a nucleoid located in the central part of the capsid covering the nucleoid and composed from capsomers, and the envelope surrounding these structures. The envelope of the particles has diverse shapes. Sometimes, it repeats a hexagonal capsid projection. Its diameter varies from 170 to 210 nm.

On the basis of on a number of generally agreeing observations, it was established that HSV-1 attachment to the cells is rather slow, and the time is difficult to measure in such cases. The virus attaches to the cells insecurely, so about 50% of the viruses can be detached in various ways.

At the adsorption site, the cell wall forms kind of a “pocket” that transforms into a vacuole, and thus the virus finds itself in a cytoplasm. Then the process of virus disintegration follows resulting in release of the nucleic acid from the proteins of the external envelopes. It is known that the perinuclear space is connected with the extracellular channel system of the endoplasmic reticulum. It is considered that in the period of cell infection, with the centripetal motion of the virus, the channels can serve as natural “passages” for the causative agent, and the structures described by various authors and called vacuoles are nothing but individual sections of the endoplasmic reticulum channels in the cross-section. In 10–12 h postinfection, the characteristic signs of virus formation are undetectable. At the same time, structural viral proteins and nuclear acids are generated to be later used to arrange the nucleic acid and the capsomers into a single structure conventionally called a nucleocapsid or a virinucleon.

The development of herpes is accompanied by the formation of intranuclear inclusions. These formations are considered as assembly sites of viral particles.

HSV-1 causes gradual suppression of macromolecular syntheses in the cell. Suppression of the cell DNA synthesis starts approximately 2 h from the onset of the disease and completes by 7 h. In HSV-1-infected HEP-2 cells, the bulk of the viral DNA is synthesized between the 3rd and the 7th hours from the onset of the disease. It was shown that the DNA of the herpes virus family is reduced in a semiconservative way. To initiate synthesis of the viral DNA, synthesis of early proteins is necessary. After the start of viral DNA synthesis, it continues in the absence of accompanying protein synthesis.



The intranuclear cycle of virus reproduction is completed with its “maturation”. Morphologically, it is expressed by covering the capsid with an envelope that further probably has a protective function.

Mass release of virus particles from the cell occurs from 15 to 18 h and is accompanied by the formation of numerous structures of a platy type. At late stages of the disease, various types of viral particles at different stages of formation get beyond the cell limits during its destruction.

## 7.2. Speckle control procedures

The experiments were conducted in a liquid thermostat of 3LI-1125M type with the optical device shown in **Figure 5** inside. Monolayers of cultured virus-free and herpes simplex virus-infected cells were the research targets. Two identical optical cuvettes were prepared for the study. There were two identical substrates in each cuvette, one with the cells and the other cell-free with nutrient solution. The experiments used HSV-1 infectious titre 4.5 lg TCD 50/ml (tissue cytopathic doses) in a dilution of  $10^{-3}$ . Speckle dynamics films of frequency 25 Hz lasting 20–40 s were recorded in the first experiments for 18–20 h at half-hour intervals. Cells of L41 line were the research target. Typical joint dependences  $\eta(t)$  for the nutrient solution and virus-free and virus-infected cells are shown in **Figure 20**.

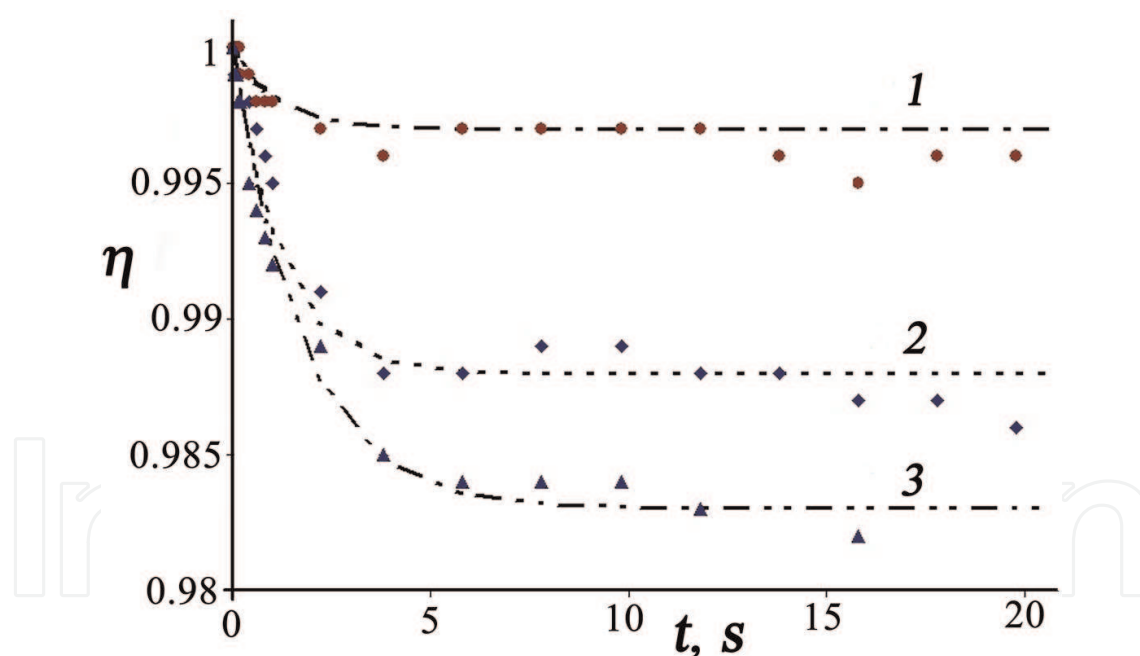


**Figure 20.** Typical joint dependences  $\eta(t)$  for the nutrient solution (1), virus-free cells (2), and virus-infected cells (3).

Analysis of dependences of  $\eta(t)$  as well as  $\sigma_u(t)$  for virus-free and virus-infected cells shows that they have features agreeing with some phases of virus development in cultured cells, but they are reproduced in about 50% of the cases. The result obtained was probably related to two considerations. First, while dependences  $\eta(t)$  were being recorded, the initial frame, starting from the second film, did not correspond to the experiment start. Second, the optical wave path variation could have been caused by several factors with relaxation times of the same

order. Appearance and disappearance of these factors could have occurred in an unpredictable mode. To eliminate the detected flaw, we altered the experimental technique. In the new technique, the program for real-time recording of dependences  $\tilde{I}(t)$  and  $\eta(t)$  was started 1 h after the administration of the virus. Values  $\tilde{I}$  were determined in preselected pixels, and value  $\eta$  was obtained by a segment of  $10 \times 10$ -pixel size in the neighborhood of the selected pixel. In 18–20 h, the program was switched off. The frame exposure time was taken as a value exceeding the radiation intensity correlation time found by the graphs in **Figure 20** and equalled 9 s.

### 7.3. Studies using L41, Vero, and HLE cells

The studies using the upgraded technique were conducted using three cell types: L41, Vero, and HLE-3. Dependences  $\tilde{I}(t)$  and  $\eta(t)$  of the nutrient solution, virus-free and virus-infected cells were considerably different for all the cell types and were well reproduced in a qualitative sense.

**Figure 21** shows typical dependences  $\tilde{I}(t)$  for the monolayer of HLE-3 cells.

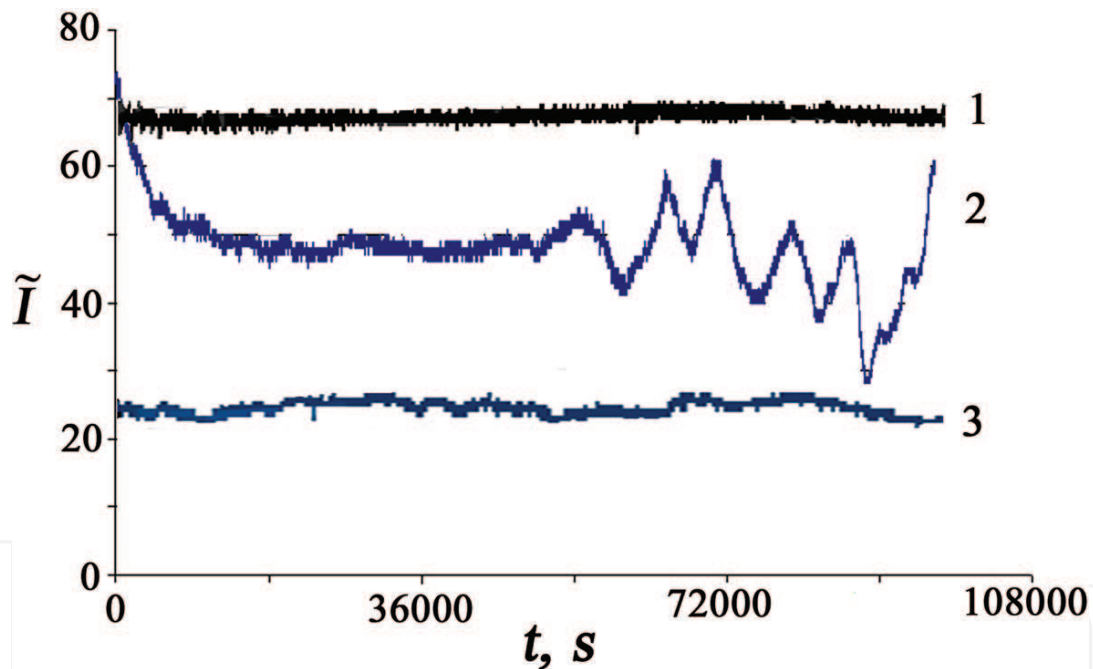


**Figure 21.** A typical dependence of  $\tilde{I}(t)$  of the HLE-3 line: (1) for the nutrient solution, (2) cells with virus, (3) for the cells without virus.

It is seen from the dependence for virus-infected cells that in the first 3 h, value  $\tilde{I}$  diminishes considerably to a certain level. This time coincides with the time necessary for penetration of the viral material into the cell and then into its nucleus. Then in the next 5 h, relatively weak fluctuations of value  $\tilde{I}$  compared with the variations of  $\tilde{I}$  occurring in the virus-free cell take place. This time interval coincides with the time interval during which the cell produces proteins necessary for appearance of new viruses. Then relatively strong quasiperiodic variations of value  $\tilde{I}$  reappear. It is known that in this time interval, a capsule with new virions grows.

In **Figures 22–24** typical dependences  $\eta(t)$  for L41, Vero, and HLE-3 cells are shown.

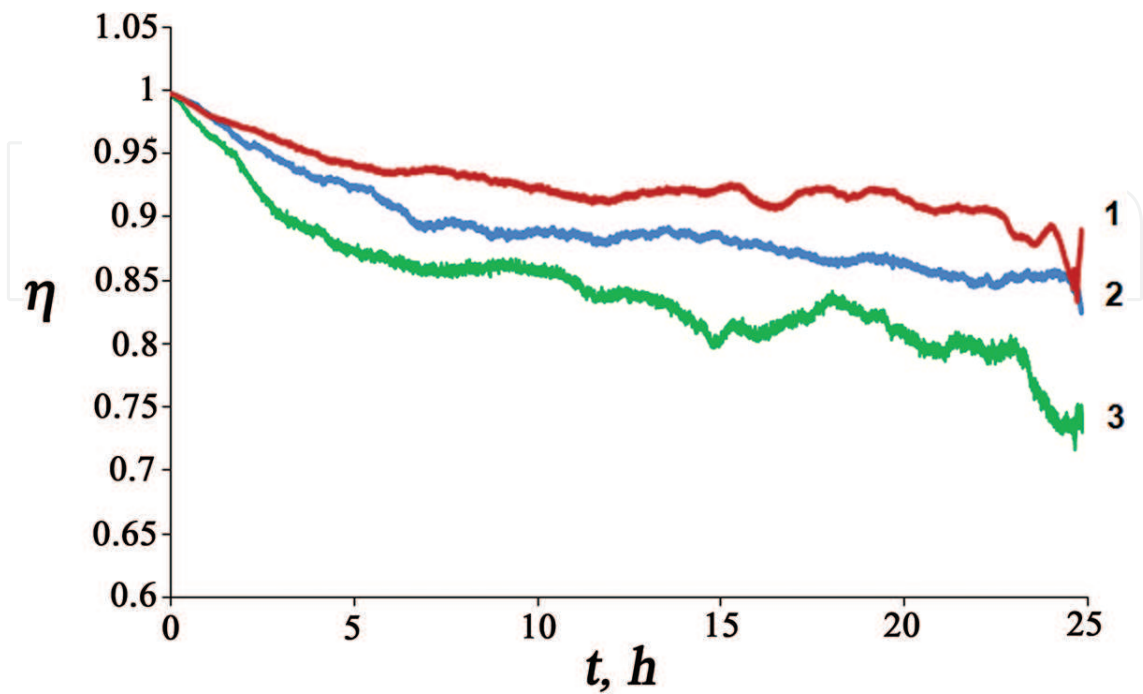


**Figure 22.** Typical dependences  $\eta(t)$  for L41 line: (1) nutrient solution, (2) cells without virus, (3) cells with virus.

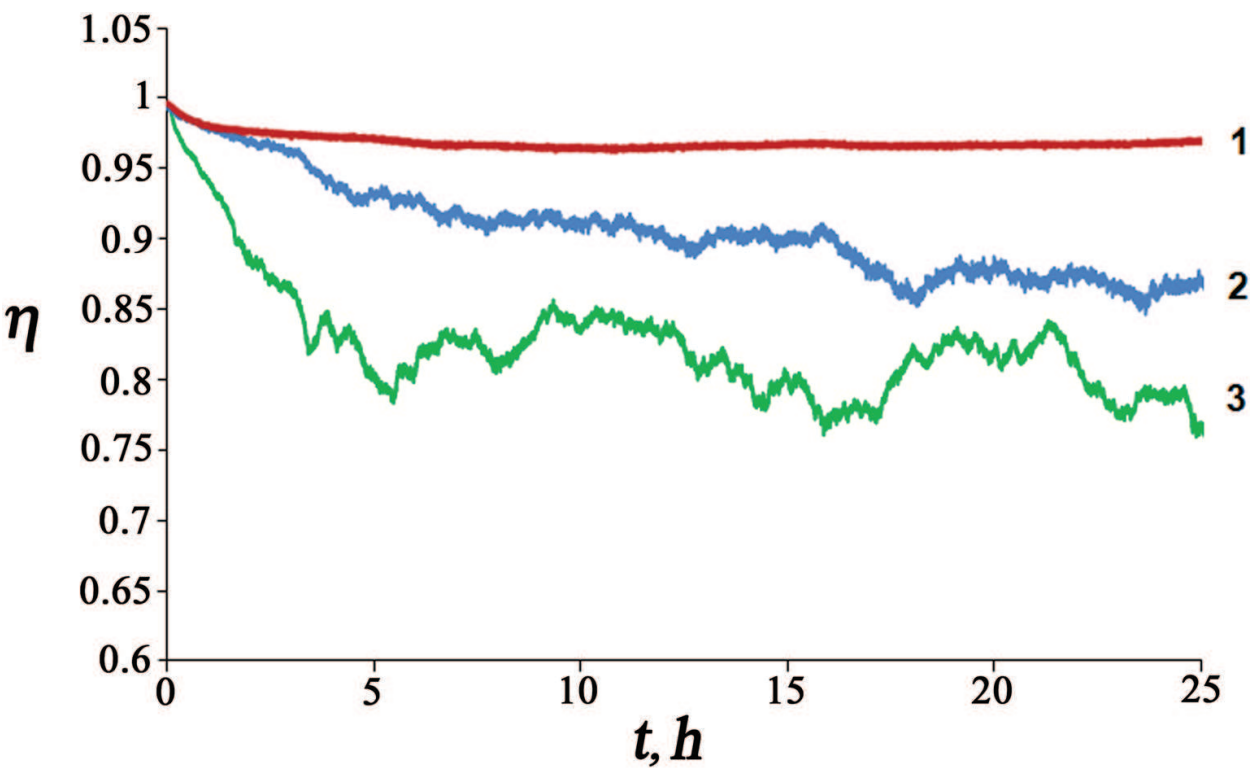


**Figure 23.** Typical dependences  $\eta(t)$  for Vero line: (1) nutrient solution, (2) cells without virus, (3) cells with virus.

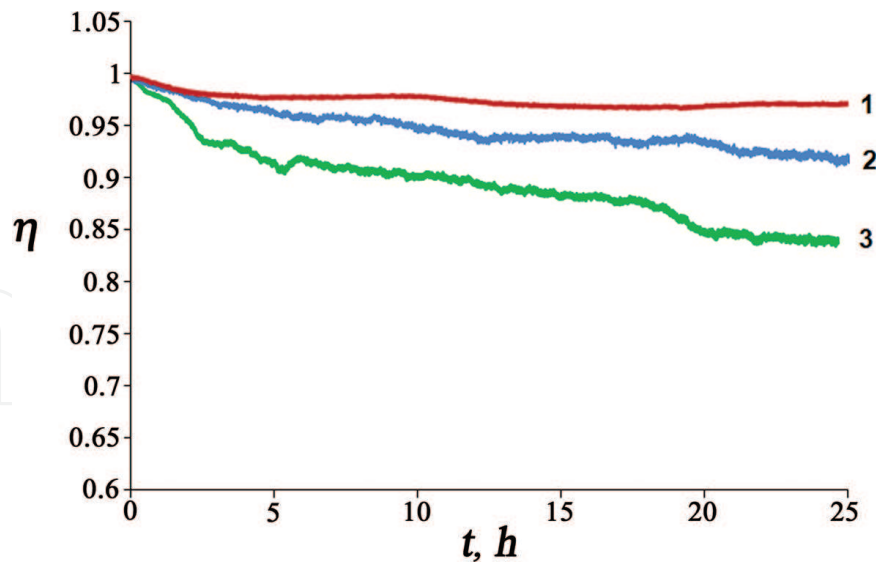


**Figure 24.** Typical dependences  $\eta(t)$  for HLE-3 sells: (1) nutrient solution, (2) cells without virus, (3) cells with virus.

Every picture presents three graphs corresponding to the nutrient solution, virus-free and virus-infected cells. It is seen from the pictures that dependences (1), (2), and (3) differ considerably in the numerical sense. Dependences (2) and (3) are nonstationary processes, but their forms are similar: first value  $\eta$  decreases rapidly, then its decrease slows down. Respectively,  $\sigma_u$  found by Eq. (30) supposing that  $\langle x_1 \rangle = \langle x_2 \rangle$  first rapidly grows, and then its growth slows down. We evaluated the multiple correlation coefficient of three masses  $\eta(t)$  corresponding to one cell type, and also to different virus-free and virus-infected cell types. For the three masses, the coefficient was in the range from 0.82 to 0.96. This character of curves  $\eta(t)$  was probably related with the fact that in the solution, the amount of nutrients gradually decreases and the concentration of harmful cell activity products increases.

Analysis of dependences  $\eta(t)$  enabled us to conclude that the presence of the virus can be reliably detected by the curve difference for virus-free cells  $\eta_1(t)$  and for virus-infected cells  $\eta_2(t)$  10 min from the experiment start. Twofold excess of the noise amplitude by difference  $\eta_1 - \eta_2$  at fixed  $t$  was considered the reliability criterion.

#### 7.4. Conclusions

The conducted experiments showed that recording of dependences  $\tilde{I}(t)$  and  $\eta(t)$  in the image plane of a cell monolayer on a transparent substrate permits reliable recording of difference in the virus-free and virus-infected cell activity. The necessary conditions are the following:

- Rigidity of the optical system providing the value of speckle image fragment correlation coefficient in the absence of the object at 0.99 level for 2 min.
- Maintenance of invariable cuvette temperature selected in the 30–37°C range with  $\pm 0.1^\circ\text{C}$  precision.
- Averaging time of radiation intensity equal to 9 s.

## 8. On some application perspectives of the technique

On the basis of the material discussed above, we can conclude that a dynamic speckle interferometry technique that allows studies of processes in thin transparent biological media has been theoretically substantiated and experimentally tested. Application of the technique is based on the formulas relating the parameters characterizing the target of research and the dynamics of speckle fields. The parameters characterizing the object are mean value  $\langle x \rangle$ , dispersion  $\sigma_u$ , and relaxation time  $\tau_0$  of the optical path difference  $\Delta u$  of sounding wave pairs as well as temporal energetic spectrum of a random process  $\Delta u = \Delta u(t)$ . The minimum sizes of the averaging regions of the above-named values are transverse and longitudinal resolution of the lens generating the object image. The parameters characterizing speckle dynamics are time-average radiation intensity  $\tilde{I}$  at a point in the image plane, relaxation time  $\tau_k$  of value  $\tilde{I}$ , constant level  $\eta^*$  of temporal autocorrelation function  $\eta = \eta(t)$  of process  $\tilde{I} = \tilde{I}(t)$ , and also the temporal energetic spectrum of this process.

Using samples in the form of a cell monolayer cultured on a transparent substrate, or one precipitated on a transparent substrate after defrosting, we demonstrated that value  $\sigma_u$  can be used as a parameter that quantitatively characterizes the activity of live cell. A technique for calibration of a relevant device and a technique for determination of value  $\sigma_u$  were developed. So applications related to assessment of cell activity can be the nearest perspective for the application of the technique. In particular, the technique for determining  $\sigma_u$  can be applied to study of the effect of toxic substances on live cells and determine their science-based maximum allowable doses. Such a technique can be applied to search the optimum drugs preventing penetration of viruses and bacteria into cells.

Determination of value  $\sigma_u$  is based on creating special conditions excluding the influence of parameters  $\langle x \rangle$  and  $\tau_0$  on speckle dynamics. In the general case, the necessity may arise for simultaneous determination of all the three parameters characterizing the processes occurring in different parts of the same cell. Further studies are needed to solve this problem.

## 9. Conclusion

On the basis of the model accounting interference of multiple waves with random phases a relation between phase dynamics of the waves sounding a thin transparent object and the speckle dynamics in the object image plane was detected theoretically. General-case formulas were obtained to determine the dependence of time-average intensity  $\tilde{I}$  and temporal autocorrelation function  $\eta = \eta(t)$  of this intensity at some point in the image plane with mean value  $\langle x \rangle$ , mean square deviation  $\sigma_u$ , and correlation time  $\tau_0$  of optical path difference  $\Delta u$  of wave pairs in the neighborhood of the conjugate point of the object plane. The diameter of this neighborhood equals the linear resolution of the lens that generates the object image. Relation between the temporal spectral function of a random process  $\Delta u(t)$  and a similar function of the process  $\tilde{I}(t)$  was substantiated.



An optical device relevant to the model used in the theory was developed.

Very good coincidence between the theory and the experiment has been demonstrated by batched random variation of path difference  $\Delta u$ . The procedure of calibrating the optical device for determination of  $\sigma_u$  was developed; its errors and the sensitivity limit of the technique were assessed.

Biological objects in the form of a live cell monolayer on a transparent substrate in a thin cuvette with nutrient solution were used to substantiate application of value  $\sigma_u$  as a cell activity parameter.

It was shown that the technique allows detection of herpes virus in cells as early as 10 min from the experiment start.

Rapid assessment of cell reaction to toxic substances therapeutic management of antibacterial and antiviral drugs can be the nearest perspective for application of the technique. Development of a technique for simultaneous determination of values  $\langle x \rangle$ ,  $\sigma_u$ , and  $\tau_0$  in different parts of an individual cell can become a line of further research.

## Acknowledgements

The authors thank the management of Yekaterinburg Research Institute of Viral Infections for aid in writing this manuscript. The authors are also grateful to Yu. A. Mikhailova for technical assistance in its preparation.

## Author details

Alexander P. Vladimirov\* and Alexey A. Bakharev

\*Address all correspondence to: [vap52@bk.ru](mailto:vap52@bk.ru)

Yekaterinburg Research Institute of Viral Infections, Yekaterinburg, Russia

## References

- [1] Goldfischer L I. Autocorrelation function and power spectral density of laser-produced speckle patterns. *Journal of the Optical Society of America*. 1965;55(3):247–253.
- [2] Enloe L H. Noise like structures in the image of diffusely reflecting objects in coherent illumination. *The Bell System Technical Journal*. 1967;(7):1479–1489.
- [3] Goodman J W. Statistical properties of laser speckle patterns. *Laser Speckle and Related Phenomena*. 1975;(9):9–75.

- [4] Goodman J W. Statistical Optics. New-York: Wiley Classics Library Edition published. 2000; 1985. 567p.
- [5] Anisimov I V, Kozel S M, Lokshin G R. Space-time statistical properties of coherent radiation scattered by a moving diffuse reflector. *Optics and spectroscopy*. 1969;27(3):483–491.
- [6] Yoshimura T. Statistical properties of dynamic speckles. *Journal of the Optical Society of America*. 1986;3(7):1032–1054.
- [7] Yamaguchi I. Speckle displacement and decorrelation in the diffraction and image fields for small object deformation. *Optica Acta*. 1981;28(10):1359–1376. DOI: 10.1080/713820454
- [8] Aleksandrov E B, Bonch-Bruevich A M. Investigation of surface strains by the hologram technique. *Soviet Physics-Technical Papers*. 1967;12:258–265.
- [9] Leendertz J A. Interferometric displacement measurement on scattering surfaces utilizing speckle effect. *Journal of Physics E: Scientific Instruments*. 1970;3(3):214–218.
- [10] Vladimirov A P, Mikushin V I. Interferometric determination of vector components of relative displacements: theory and experiment. In: Tuchin V V, Ryabukho V P, Zimnyakov D A, editors. *Saratov Fall Meeting '98: Light Scattering Technologies For Mechanics, Biomedicine, and Material Science; 06-09 October 1998; Saratov Bellingham (USA): SPIE; 1999. pp. 38–43. DOI: 10.1117/12.341416*
- [11] Rabal H J, Braga R A, editors. *Dynamic Laser Speckle and Applications*. New York: CRC Press; 2008. 282p.
- [12] Briers J D, Fercher A F. Retinal blood-flow visualization by means of laser speckle photography. *Investigative Ophthalmology and Visual Science*. 1982;22(2):255–259.
- [13] Briers J D. Laser speckle contrast imaging for measuring blood flow. *Optica Applicata*. 2007;37(1-2):139–152.
- [14] Ansari M Z, Humeau-Heurtier A, Offenhauser N, Drier J P, Nirala A K. Visualization of perfusion changes with laser speckle contrast imaging using the method of motion history image. *Microvascular Research*. 2016;107:106–109. DOI: 10.1016/j.mvr.2016.06.003
- [15] Maxwell J C. *Treatise on electricity and magnetism*. Moscow: Nauka; 1989. 416p.
- [16] Landau L D, Lifshitz E M. *The Classical Theory of Fields*. 1st ed. USA: Addison-Wesley; 1951. 425p.
- [17] Landsberg G S. *Optica*. 6th ed. Moscow: Fizmatlit; 2003. 848p.
- [18] Ginzburg V M, Stepanov V M, editors. *Holography. The methods and apparatus*. Moscow: Soviet radio; 1974. 376p.
- [19] Born M, Wolf E, editors. *Electromagnetic Theory of Propagation, Interference and Diffraction of Light*. 7th ed. Cambridge: Cambridge University Press; 1999. 952p.
- [20] Ryabukho V P. Diffraction of interference fields on random phase objects. In: Tuchin V V, editor. *Coherent-Domain Optical Methods: Biomedical Diagnostics, Environmental and*

Material Science. 1st ed. Boston, Dordrecht, London: Kluwer Academic Publishers; 2004. pp. 235–318.

- [21] Bakut P A, Mandrosoy V I, Matveyev I N, Ustinov N D. Theory of coherent images. Moscow: Radio and communication; 1987. 264p.
- [22] Vladimirov A P. Three-dimensional diffuser and three-dimensional speckles. Technical physics. 1998;43(12):1454–1458.
- [23] Vladimirov A P. Dynamic speckle interferometry of bodies under deformation. Yekaterinburg: UrO RAN Publ.; 2004. 241p.
- [24] Hauf V, Grigul U. Optical methods in heat transfer. Moscow: Mir; 1973. 240p.
- [25] Vasilyev L A. The shadow methods. Moscow: Nauka; 1968. 400p.
- [26] Fomin N A. Speckle Photography for Fluid Mechanics Measurements. 1st ed. Berlin: Springer-Verlag; 1998. 219p.
- [27] Jakeman E. Photon correlation. In: Cummins H Z, Pike E R, editors. Photon Correlation and Light Beating. 1st ed. New-York: Springer Science+Business Media; 1974. pp. 75–149.
- [28] Vladimirov A P. Speckle dynamics in the image plane of a plastically deformable object [dissertation]. Sverdlovsk: Institute of metal physics; 1989. 106p.
- [29] Vladimirov A P, Druzhinin A V, Malygin A S, Mikitas K N. Theory and calibration of speckle dynamics of phase object. Proceedings of SPIE. 2012;8337(83370C): 1–15.
- [30] Vladimirov A P. Dynamic speckle interferometry of microscopic processes in thin biological objects. Radiophysics and Quantum Electronics. 2015;57(8):564–576.
- [31] The State System of Measurements. Indirect Measurements. Determination of Measurement Results and Estimation of their Errors MI 2083–90. Moscow. 1991.
- [32] Bakharev A A, Burygina N A, Vissarionov VA, Glinskih N P, Karpova E I, Malyushenko O I. Patent RU 2148644: Method of control of the cytotoxicity of the gel using a strain of transplantable human leukocytes L41 CD/84. 1998.
- [33] Malygin A S, Bebenina N V, Vladimirov A P, Mikitas K N, Baharev A A. A speckle - interferometric device for studying the cell biological activity. Instruments and experimental techniques. 2012;55(3):415–418.
- [34] Barinskij I F, Shubladze A K, Kasparov A A, Gribenyuk S V. Herpes (etiology, diagnosis, treatment). Moscow: Medicina; 1986. 351p.

